University of Geneva
D.P.N.C

Master Thesis

Electron Muon Ranger (EMR) Hardware Characterization

Author:
François DRIELSMA

Supervisor:
Pr. Alain BLONDEL

Assistants:
Ruslan ASFANDIYAROV
Yordan KARADZHOV

June 19, 2014

Abstract

The Electron Muon Ranger (EMR) is a totally active scintillator which purpose is the electron background rejection downstream the cooling channel at the international Muon Ionization Cooling Experiment. It consists in 2832 plastic scintillator bars divided in 48 planes in an X-Y arrangement and uses particle range reconstruction as its main variable to tag muons and discriminate electrons.

In the context of a Master Thesis, several short analyses were conducted to characterize the hardware of the EMR and determine if everything is working as designed. All the results were beyond satisfactory as, even though 4 channels (0.15 % of the detector) are dead, the entirety of the electronics work perfectly and every last one of the 5664 clear fibres coming from the bars gives out a good amount of light. Two channels were found mismatched and the DAQ channel map was subsequently corrected. The level of crosstalk was within range for the type of Multi Anode PMT used with less than 0.5 % likelihood of crosstalk in most of the channels and an average of 4.5 ± 1.5 % of the initial channel intensity measured upon occurrence. The efficiency of the signal acquisition, defined as the probability of recording a signal in a plane when a particle goes through it in beam conditions, reaches 99.73 ± 0.02 %.

Contents

Introduction

More than 80 years have passed since Pauli first postulated the existence of the neutrino to *save the law of conservation of energy* in his famous letter. A little over 25 years later, Cowan and Reines eventually confirmed its existence and a new era in particle physics was born. Six fascinating decades of neutrino research ensued. The first concern was to determine its characteristics to classify its role and place in the mainstream theories. In the 70s and 80s, the neutrino was used to investigate the nature of the weak interaction and probe the nucleon structure. Now, in the last three decades, the focus has fallen back to its roots: the nature of the three generations of neutrinos, their mass scale, their mixing and their oscillations. In modern particle physics, this field of research is exciting and constantly moving because it remains on the edge of the almighty Standard Model that incorrectly predicts massless neutrinos.

Despite the continuous international effort, a lot of questions remain unanswered when it comes to this *ghost particle* that is the neutrino. A good part of the oscillation parameters is inaccurately known while its potential leptonic CP violation and its mass eigenstates ordering remain undiscovered. The Neutrino Factory (NuFact) collaboration, which studies the feasibility and design of such a facility since the beginning of the 21^{st} century, has taken upon itself to answer most of them in a single worldwide experiment. The idea behind this great machine involves a very high luminosity collimated muon storage ring as a source of intense and perfectly pure neutrino beams, a near and a far detector to observe the neutrino oscillations from different baselines and beam tunings.

One of the main challenges to achieve such a device is the development of an operational muon cooling channel. The muons, produced from the decay of pions, can't be accelerated efficiently without reducing their transverse emittance first. The international Muon Ionization Cooling Experiment (MICE) collaboration intends to experimentally demonstrate that the use of ionization cooling as the key stone of the Neutrino Factory cooling channel is a viable solution. The experiment is currently ongoing and should yield its first results with an absorber in 2015. To put it in numbers, the collaboration is trying to observe a 10 % reduction in the beam emittance with a short cooling channel.

MICE has invoked several existing detector technologies to be able to measure the effect of ionization cooling on a muon beam; these detectors are necessary to measure the beam emittance at the entrance and at the exit of the channel and to reject the particle background. The latter task is tricky and has called upon the help of a calorimeter to discriminate the electron background downstream the cooling channel, a key element of which is the Electron Muon Ranger (EMR). The EMR is a 1.5 tons Fully Active Scintillator detector composed of 2832 scintillating bars divided in 48 planes. It uses the particle range reconstruction as a powerful tool to highlight the muon tracks.

Naturally following the implementation of the EMR in the MICE beamline in October 2013, this Master Thesis intends to investigate the performance of the EMR hardware in working conditions. A brief summary of the motivations behind this experiment, its design choices and the conception of the EMR is proposed at first. The analyses are then presented chronologically, starting with the tests performed during construction and ending with channel mismatch, crosstalk, misalignment and efficiency investigations of the whole detector.

1 Current status in Neutrino Physics

Neutrinos are spin 1/2 electrically neutral particles with a very light mass (in the order of ~ 500000 times smaller than the electron mass [1]) and are the most abundant particles in the universe. The three known neutrino types, or flavours, (ν_e , ν_μ and ν_τ) interact weakly with matter via the weak bosons $W^\pm, Z^0$. They stem from various sources, both natural and artificial.

The strongest nearby neutrino source is the Sun: the fusion reaction in which hydrogen is transformed into helium ($2H \rightarrow {}^4He$) produces $\sim 2 \times 10^{39}$ electron neutrinos per second which corresponds to a $6 \times 10^{10}\, \nu/cm^2 s$ flux at the Earth's surface [2]. A huge amount of neutrinos (up to $\sim 10^{58}$ neutrinos in a few seconds) are also produced in Supernovae explosions [3] while relic neutrinos (the so-called Cosmic neutrino Background, a.k.a. CνB [4]) fill the Universe with a density of $\sim 100\, \nu/cm^3$.

Neutrinos are also produced on Earth both in the surrounding atmosphere and in its crust. The hadronic showers induced by the interaction of cosmic rays with the high layer of the atmosphere generate a typical flux of $\sim 1\, \nu/cm^2 s$ at the Earth's surface [5] while geoneutrinos are produced through the -decay process of radioactive nuclei (typically ${}^{238}U$, ${}^{232}Th$ and ${}^{40}K$) with a flux of $\sim 107\, \nu/cm^2 s$ [6].

Neutrinos can also be produced by artificial man-made sources: electron antineutrinos are generated with a typical flux of the order of $10^{20}\, \nu$ per second in nuclear reactors [7] while fluxes up to $105\, \nu/cm^2 s$ of ν_μ can be achieved with conventional accelerated beams by the interaction of a proton beam with a target and the subsequent decay of the produced mesons.

In this section a short summary of the current status in neutrino is presented from the historical, experimental and theoretical point of view.

1.1 History and major experiments

The first notable event in the history of neutrino can be identified with Lise Meitner and Otto Hahn's discovery (1911) of the continuous β energy spectrum, which couldn't be explained with the energy conservation law as it appeared that some energy was lost in the decay process [8], as shown in fig. 1.1 (a). Almost two decades went by before Wolfgang Pauli, in his famous open *neutrino letter* to the meeting in Tübingen, postulated the existence of a new particle, that he then called neutron, to solve the dilemma of the β decay [9].

Three years later, in 1933, Enrico Fermi already published the first account of his theory on β decay which pinnacle was in his famous weak interaction theory in 1934 [10]. The following two decades were characterized by a continuous effort to prove the existence of the neutrino and to determine its physical properties. Pauli will have to wait until 1956, 2 years before his death, to see his hunch confirmed when Clyde L. Cowans and Frederick Reines saw the first neutrino event by detecting the inverse β decay process at the Savannah River reactor [11] using the detector represented in fig. 1.1 (b).

A few years later, Maurice Goldhaber showed that neutrinos involved in the weak interaction are left-handed particles [12], while in 1962 the first evidence of the existence of different neutrino generations came from the ν_μ observation at Brookhaven [13], completed much later by the discovery of the third generation ν_τ at the FNAL in 2001 [14]. These experiments consolidated the idea of

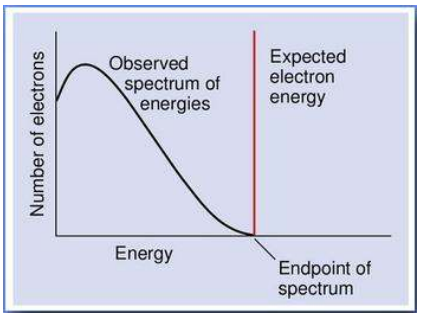

(a)

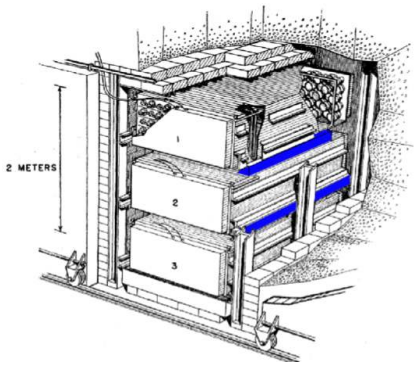

(b)

(c)

(d)

Figure 1.1: (a) Expected electron energy spectrum for a two body final state (red line) by opposition to the observed spectrum (smooth black curve). A two body final state (${}^{n}_{m}X \rightarrow {}^{n}_{m+1}X + e^{-}$) can't account for a continuous spectrum, the introduction of a third body was thus suggested [9] (${}^{n}_{m}X \rightarrow {}^{n}_{m+1}X + e^{-} + \bar{\nu}_e$). (b) Schematic layout of the detector used by Cowans and Reines to detect the neutrino [11]: it consisted of two large plastic tanks (in light blue) filled with 200 l of water mixed with CdCl2 and sandwiched between three 1400 l liquid scintillator detectors. (c) Picture of the mine that hosted the Homestake neutrino detector and tanker of perchloroethylene [15]. (d) Picture of the cave harbouring KamLAND and its main spherical liquid scintillator vessel [16]. The inner surface of the sphere is covered by 1879 50 cm PTMs.

Parameter	Best Fit	1σ range	2σ range	3σ range
Δm^2_{21} $[10^{-5}\text{eV}^2]$	7.62	$7.43 - 7.81$	$7.27 - 8.01$	$7.12 - 8.20$
$\lvert\Delta m^2_{31}\rvert$ $[10^{-3}\text{eV}^2]$	2.55 2.43	$2.46 - 2.61$ $2.37 - 2.50$	$2.38 - 2.68$ $2.29 - 2.58$	$2.31 - 2.74$ $2.21 - 2.64$
$\sin^2\theta_{12}$	0.320	$0.303 - 0.336$	$0.29 - 0.35$	$0.27 - 037$
$\sin^2\theta_{23}$	0.613 0.600	$0.573 - 0.625$ $0.569 - 0.626$	$0.38 - 0.66$ $0.39 - 0.65$	$0.36 - 0.68$ $0.37 - 0.67$
$\sin^2\theta_{13}$	0.0246 0.0250	$0.0218 - 0.0275$ $0.0223 - 0.0276$	$0.019 - 0.030$ $0.020 - 0.030$	$0.017 - 0.033$
δ	0.80π -0.03π	$0 - 2\pi$	$0 - 2\pi$	$0 - 2\pi$

Table 1.1: Neutrino oscillation parameters summary. For Δ^2_{31}, $\sin^2\theta_{23}$, $\sin^2\theta_{13}$, and δ the upper (lower) row corresponds to normal (inverted) neutrino mass hierarchy [26].

neutrino oscillations, first proposed by Bruno Pontecorvo in 1957 [17] using the same formalism as for the quark mixing, and subsequently developed by Ziro Maki, Masami Nakagawa and Shoichi Sakata in 1962 [18].

The experimental neutrino physics era truly boomed in 1968 when John Bahcall and Ray Davis first showed a non-negligible deficit in the solar neutrino flux measurement with a detector (fig. 1.1 (c)) based on Chlorine [19]. The neutrino mixing and oscillation theory was suggested to be a possible solution to the so-called Solar Neutrino Puzzle, a.k.a. SNP. In the following twenty years, the main solar neutrino experiments (Homestake [15], SAGE [20] and GALLEX [21]) confirmed the solar neutrino flux deficit observed by Davis and Bahcall, but it was only in 2002 that the SNP was solved by the Sudbury Neutrino Observatory (SNO) experiment [22]. Its unique ability to detect the three neutrino flavours and distinguish the ν_e from the other generations provided the scientific community with the final piece of evidence of solar neutrino oscillations.

At the same time, the neutrino oscillation has also been observed in the atmospheric neutrino field: an upward-downward ν_μ asymmetry was observed without a corresponding deficit in ν_e. The oscillation between the ν_μ and ν_τ was proposed as an explanation to this deficit of muon neutrinos [23].

Other experiments dedicated to the determination of the oscillation parameters have been built in the recent years, exploiting nuclear reactor neutrino production as well. The KamLAND experiment (fig. 1.1 (d)) provided several confirmations of both the solar and atmospheric neutrino oscillation results [16].

As described in more details in section 1.2, the three flavour oscillations the six relevant parameters are three mixing angles (θ_{12}, θ_{13} and θ_{23}), a CP violating phase δ and two mass-squared differences Δm^2_{21} and $|\Delta m^2_{31}|$, where $\Delta m^2_{ji} = m^2_j - m^2_i$. The oscillation parameters obtained from the two most recent global fits to the world neutrino data (e.g. T2K [24], Double Chooz [25]) are summarized in tab. 1.1 [26].

1.2 Mixing

The fact that neutrinos have masses implies that there is a spectrum of neutrino mass eigenstates ν_i, $i = 1, 2, 3$, each with a mass m_i. In turn this means that mixing among the three known neutrino flavours is possible. Mixing means that in the $W^{\pm}$ decays to the particular charged lepton l_α (antilepton $\bar{l}_\alpha$), $\alpha = e, \mu, \tau$, the accompanying neutrino mass eigenstate is not always the same ν_i , but can be any of the different ν_is.

In particular, the neutrino mixing is described by the 3×3 Pontecorvo-Maki-Nakagawa-Sakata unitary matrix U_{PMNS}, which is analogous to the CKM matrix in the quark sector [27, 28]:

$$U_{PMNS} = \begin{bmatrix} c_{12}c_{13} & s_{12}c_{13} & s_{13}e^{-i\delta} \\ -s_{12}c_{23} - c_{12}s_{23}s_{13}e^{i\delta} & c_{12}c_{23} - s_{12}s_{23}s_{13}e^{i\delta} & s_{23}c_{13} \\ s_{12}s_{23} - c_{12}c_{23}s_{13}e^{i\delta} & -c_{12}s_{23} - s_{12}c_{23}s_{13}e^{i\delta} & c_{23}c_{13} \end{bmatrix}. \quad (1.1)$$

where $c_{ij} = \cos\theta_{ij}$ and $s_{ij} = \sin\theta_{ij}$ with $i, j = 1, 2, 3$. The phase factor δ is non-zero only if the neutrino oscillation violates CP symmetry. The UPMNS matrix thus relates the mass eigenstates (ν_1, ν_2, ν_3) to the light-neutrino flavour eigenstates (ν_e, ν_μ, ν_τ).

Using the Dirac formalism, a neutrino of flavour α can be expressed as a superposition of the three mass eigenstates and vice versa through the following formulas

$$|\nu_\alpha\rangle = \sum_i U^*_{\alpha i} |\nu_i\rangle , \quad (1.2)$$

$$|\nu_i\rangle = \sum_\alpha U_{\alpha i} |\nu_\alpha\rangle . \quad (1.3)$$

Here, $U_{\alpha i}$ corresponds to the UPMNS matrix element and denotes the probability amplitude for the W^+ decay to produce the specific combination $l_\alpha + \nu_i$, i.e. the fraction of the flavour α in ν_i is $|U_{\alpha i}|^2$.

The relationship between the weak eigenstates and the mass ones through the mixing angles (θ_{12}, θ_{13} and θ_{23}) that arises from eq. 1.1 are presented in fig. 1.2

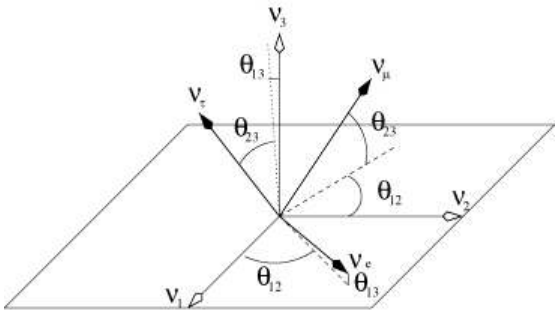

Figure 1.2: Rotation of the neutrino mass eigenstates (ν_1, ν_2, ν_3) into the flavour eigenstates (ν_e, ν_μ, ν_τ) as stated in eq. 1.1. The definitions of the Euler angles (θ_{12}, θ_{13} and θ_{23}) are also indicated [29].

1.3 Oscillation

Although the neutrino oscillation (i.e. flavour change) process is a strictly quantum-mechanical phenomenon, the oscillation probability $P(\nu_\alpha \to \nu_\beta)$, that indicates the probability of finding a neutrino created in a given flavour state to be in another one, can be derived using an efficient and simple approach that contains all the essential quantum physics. The reasoning is summarized briefly in this section and extensively developed in [30].

A typical neutrino oscillation is represented schematically in fig. 1.3. A neutrino source produces a neutrino of flavour α together with the corresponding charged antilepton $\bar{l}_\alpha$. Let us suppose it travels a distance L to a detector where it interacts with a target and produces a second charged lepton l_β. Hence, at the time of its interaction in the detector, the neutrino is a ν_β. If $\alpha \neq \beta$, the neutrino has changed from a ν_α to a ν_β while travelling from the source to the detector.

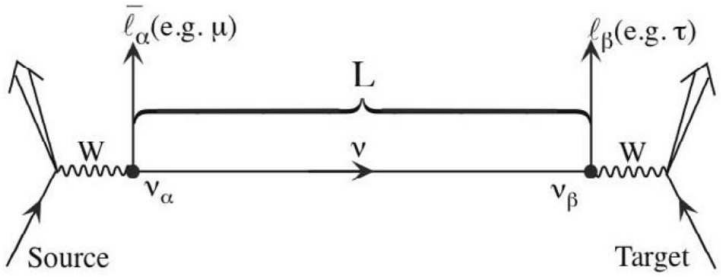

Figure 1.3: Neutrino oscillation scheme: a neutrino of flavour α travels over a distance L. When it interacts with the detector it produces a second charged lepton l_β. Hence the ν_α neutrino has oscillated into the ν_β neutrino while travelling from the source to the target. [30]

Since $|\nu_i\rangle$ are mass eigenstates, their propagation can be described by plane wave solutions of the Schrödinger equation of the form:

$$|\nu_i(t)\rangle = e^{-i(E_i t - \vec{p}_i \cdot \vec{x})}|\nu_i(0)\rangle, \tag{1.4}$$

in natural units with t the propagation time, $\vec{p_i}$ the three-momentum and $\vec{x}$ the position. E_i is the energy of the mass eigenstate i and, in the ultrarelativistic limit $|\vec{p_i}| = p_i \gg m$, reads

$$E_i = \sqrt{p_i^2 + m_i^2} \simeq p_i + \frac{m_i^2}{2p_i} \simeq E + \frac{m_i^2}{2E}, \tag{1.5}$$

where E is the total energy of the particle.

This limit applies to all practical (currently observed) neutrinos, since their masses are of order 1 eV and their energies are at least 1 MeV, the Lorentz factor γ is greater than 106 in all cases. Using also $t \simeq L$ (holds for $v \simeq c$), where L is the distance travelled and also dropping the phase factors, the wave function becomes:

$$|\nu_i(L)\rangle = e^{-im_i^2 L/2E}|\nu_i(0)\rangle. \tag{1.6}$$

As the flavour eigenstates are a linear combination of the mass ones with evolving parameters, it possible to observe a neutrino to change its flavour during its propagation. The probability that a neutrino originally of flavour α will later be observed at target having flavour β is

$$P_{\alpha\to\beta} = |\langle\nu_\beta|\nu_\alpha(t)\rangle|^2 = \left|\sum_i U^*_{\alpha i} U_{\beta i} e^{-im_i^2 L/2E}\right|^2, \tag{1.7}$$

which can be more conveniently written as

$$\begin{aligned} P_{\alpha\to\beta} = \delta_{\alpha\beta} \quad &- \quad 4\sum_{i>j} \mathrm{Re}(U^*_{\alpha i} U_{\beta i} U_{\alpha j} U^*_{\beta j}) \sin^2(\tfrac{\Delta m^2_{ij} L}{4E}) \\ &+ \quad 2\sum_{i>j} \mathrm{Im}(U^*_{\alpha i} U_{\beta i} U_{\alpha j} U^*_{\beta j}) \sin(\tfrac{\Delta m^2_{ij} L}{2E}). \end{aligned} \tag{1.8}$$

Several characteristics of the neutrinos can be drawn from this formula:

- if neutrinos are massless, i.e. $\Delta m^2_{ij} = 0$, equation 1.8 becomes $P_{\alpha\to\beta} = \delta_{\alpha\beta}$. Hence, the observation that neutrinos can change flavour implies non-degenerate neutrino masses, and in particular non-zero [30];
- the flavour change probability depends on the quantity L/E. Depending on the choice of L (known as *baseline*). Experiments can be classified in Short BaseLine (SBL) and Long BaseLine (LBL) [30];
- there are two fundamental ways to detect neutrino flavour oscillations: *appearance* and *disappearance* experiments [30]. In a beam of neutrinos which are initially all of flavour α , the observation of neutrinos of a new flavour β (*appearance*) or of a ν_α flux reduction (*disappearance*) are both possible;
- the neutrino oscillation probability depends only on the neutrino squared mass splittings Δm^2_{ij} and not on the individual neutrino masses [30]. Oscillation experiments can thus determine the neutrino squared-mass spectral patterns, but not how far above zero the entire spectrum lies. Two possibilities for the mass ordering are foreseen: the situation where $m_3 > m_2 > m_1$, known as direct (or normal) hierarchy while the inverse hierarchy is given by $m_2 > m_1 > m_3$.

Both the results from solar and atmospheric neutrinos have shown that a simplified two-flavour approximation can be an accurate description for several sets of data. In this simplest case of two neutrino mixing between ν_α, ν_β and ν_1, ν_2, there is only one squared-mass difference $\Delta m^2_{12} = \Delta m^2 = m_1^2 - m_2^2$ and the mixing matrix U can be parametrized in terms of only one mixing angle θ:

$$U = \begin{pmatrix} \cos\theta & \sin\theta \\ -\sin\theta & \cos\theta \end{pmatrix}. \tag{1.9}$$

The resulting survival probability of a given flavour can be written as

$$P_{\alpha\to\alpha} = 1 - \sin^2(2\theta)\,\sin^2\left(1.267\frac{\Delta m^2 L}{E}\frac{\mathrm{GeV}}{\mathrm{eV^2\,km}}\right). \tag{1.10}$$

where $\sin^2 2\theta$ is the oscillation amplitude. The survival probability of a 1 GeV muon neutrino is plotted in fig. 1.4 as a function of flight distance L.

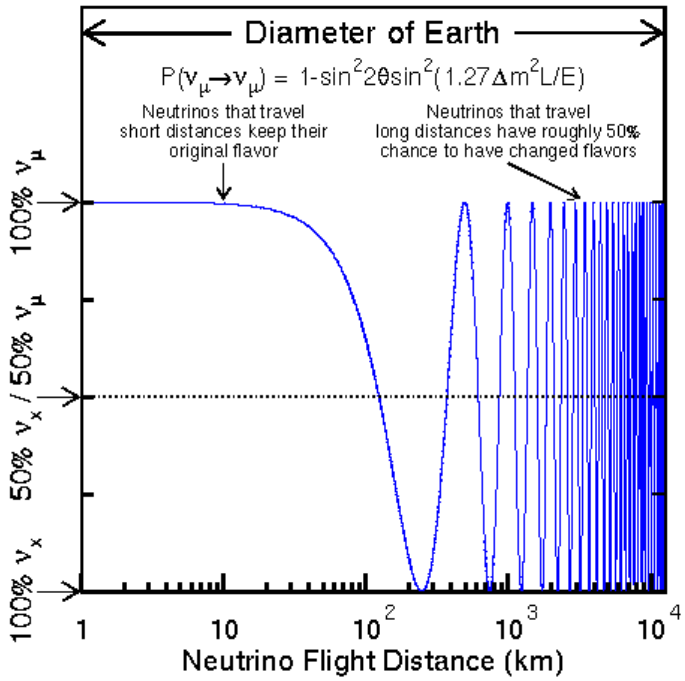

Figure 1.4: Survival probability of a ν_μ as a function of the flight distance L. Provided an appropriate choice of baseline, it is possible to observe a lower flux of ν_μs than predicted (disappearance).

2 International Muon Ionization Cooling Experiment

Particle physics experiments based on muon acceleration have been the object of increasing interest in the last 20 years. A Neutrino Factory based on a high energy muon storage ring is the ultimate tool to study the neutrino mixing parameters [31] summarized in tab. 1.1. This type of facility also provides the best chance of discovering and studying accurately the leptonic CP violation. In addition, the potential outcome of a Neutrino Factory goes beyond its own results as it would pave the way to a brand new line of high brilliance muon accelerators and a take the first step towards a muon collider [32], potential candidate of choice for a multi-TeV lepton-antilepton collisions.

A Neutrino Factory could be built using accessible technologies, with a performance matching the requirements of an exciting physics program. Cost estimates, however, are quite high ($1.9 billion in US Feasibility Study II [33]), and several of the techniques considered have never been applied in practise. A sizeable programme of R&D is thus required to lower the costs and investigate new technologies.

In the uncharted territory that lays on the path to a functional Neutrino Factory, the ionization cooling is allegedly the largest novelty in accelerator physics. Ionization cooling of muons at minimum-ionizing energy has never been realised in practise and has yet to be demonstrated. Nevertheless, it makes significant contributions to both the performance (up to a factor of 10 in neutrino intensity [34]) and cost (as much as 20% [33]) of a Neutrino Factory. This motivates the proposal of a muon ionization cooling experiment.

The international Muon Ionization Cooling Experiment (MICE) collaboration has been created to carry out this program. It consists of accelerator physicists and experimental particle physicists from Europe, Japan and the US. The goals of the experiment are:

- to build a section of a cooling channel that is long enough to provide a measurable cooling effect (up to 10% reduction in transverse emittance) but short enough to be affordable and flexible enough to allow a variety of beam momenta, optics and absorbers to be investigated;
- to use particle detectors to measure the cooling effect with high precision, achieving an absolute accuracy on the measurement of emittance of 0.1% or better;
- to perform measurements in a muon beam with momentum in the range $140 - 240$ MeV/c. The beam intensity will be such that a single particle will pass through the experiment every 100 ns or so.

In this section, we will develop briefly the appeal of the Neutrino Factory physics and its concepts, the ionization cooling technique and the design of the MICE cooling channel at RAL.

2.1 Neutrino factory

2.1.1 Physics

The potential of a Neutrino Factory is unprecedented in neutrino physics [31]. It could provide measurements of the the neutrino mixing matrix elements as well as the neutrino oscillation ones with an unchallenged precision. Moreover, it would have a high enough resolution to unravel a potential leptonic CP violation [35] and the connected studies of slow muon physics would open the way to a muon collider at extremely high energy [32].

A muon storage ring providing neutrino beams is the ultimate tool for the measurement of the U_{PMNS} elements, simply because it can offer a well defined energy spectrum as well as a high purity beam. On the one hand, the flavour composition of the beam is well known and the beam is focused and intense and, on the other, the production of very high energy ν_es allows the study of the $\nu_e \to \nu_\tau$ mixing channel [31].

The other fundamental goal of a Neutrino Factory is to measure the oscillation parameters with a very high precision [31] (current values are summarized in tab. 1.1):

- very precise measurement of Δm^2_{23} and θ_{23};
- measurement of the small mixing angle θ_{13} with a precision better than half a degree;
- the determination ordering of neutrino masses, i.e. the sign of Δm^2_{23} made possible by the MSW effect[1] on the neutrinos during their passage through the earth and its influence on the ratio $\mathcal{R} = N(\nu_e \to \nu_\mu)/N(\bar{\nu}_e \to \bar{\nu}_\mu)$;
- search for CP violation through the precise measurement of the same appearance rate asymmetry $\mathcal{R}$ as function of the energy E and baseline L.

Fig. 2.1 (a) shows the predicted ratio $\mathcal{R} = N(\nu_e \to \nu_\mu)/N(\bar{\nu}_e \to \bar{\nu}_\mu)$ as a function of the baseline [29]. At very short baselines ($L \simeq 0$), neither the matter effects nor the CP violation influence the appearance rate: the ratio is 0.5 which reflects the different neutrino and antineutrino cross sections. As the baseline is chosen to be more remote, the ratio $\mathcal{R}$ increases (decreases) thanks to the MSW effect if the sign of the mass splitting Δm^2_{23} is negative (positive). At long baseline, the CP violation enters in the equation and influences the ratio slightly (indicated by the light red bands). The high precision measurements of $\mathcal{R}$ will provide both the sign of Δm^2_{23} and the CP phase δ determination.

The Neutrino Factory physics potential in terms of the small angle $\sin^2\theta_{13}$ sensitivity has been estimated in comparison with the major considered neutrino experiments [37]. The alternatives to this facility include JHF-SK, a combination of the Japan Proton Accelerator Research Complex 50 GeV proton driven superbeam with the existing SuperKamiokande detector [38] and the similar JPARC-HK with the proposed HyperKamiokande detector [39]. Fig. 2.1 (b)

[1] The MSW (Mikheyev-Smirnov-Wolfenstein) effect is the effect of transformation of one neutrino species (flavour) into another one in a medium with varying density. Three basic elements of the effect include: the refraction of neutrinos in matter, the resonance (level crossing) and the adiabaticity. The effect depends on the neutrino masses hierarchy [36].

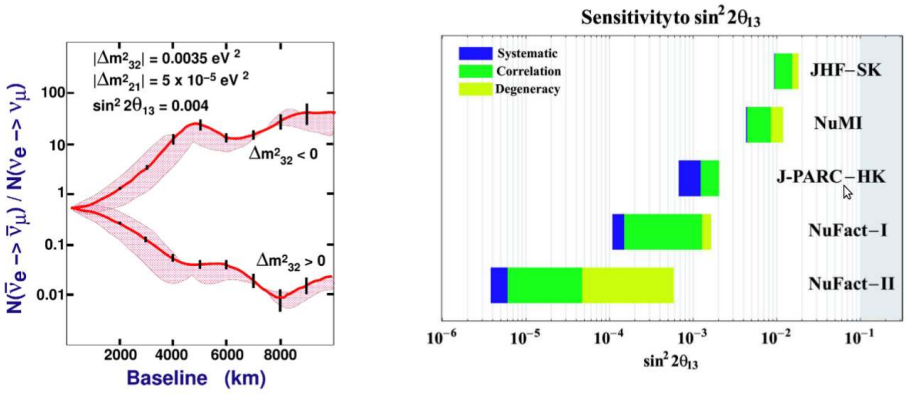

(a) (b)

Figure 2.1: (a) Event rate $\mathcal{R} = N(\nu_e \to \nu_\mu)/N(\bar{\nu}_e \to \bar{\nu}_\mu)$ as a function of the baseline [29]. The two possibilities of positive and negative Δm^2_{23} are shown together with the variation of the CP phase (indicated by the light red bands). (b) Sensitivity of *entry-level* and high-performance Neutrino Factory (NuFact I and II respectively) to $\sin^2\theta_{13}$ in comparison with that of other proposed facilities [29].

summarizes the superiority of the Neutrino Factory over any other combination of beams and detectors. The left end of the bars indicates the statistical sensitivity limit; it is reduced if the correlations with other oscillation parameters and degeneracy errors are included. Fortunately, these additional sources of error can be addressed and the final achievable sensitivity is given by the leftmost edge: in both cases a fully developed Neutrino Factory overcomes the sensitivity of the other experiments by up to two orders of magnitude.

In addition of the high precision measurements of the mixing and oscillations parameters, a Neutrino Factory also offers the possibility to study several other physics fields, from the measurements of the QCD parameters to the investigation of the electroweak sector of the Standard Model.

Precise measurements of the Deep Inelastic Scattering (DIS) neutrino physics will be made possible by the use of a Neutrino Factory [31]. Moreover, the electroweak sector of the Standard Model, in particular the determination of $\sin^2\theta_W$, could be tested from the measurements of both electron and muon neutrino cross sections [31]. Finally, non-neutrino science would also be possible; intense beams of muons with momenta of $\sim$ 100 MeV/c and a variety of time structures can be provided and slow muon physics studies can be performed with sufficiently high statistics. Both muon lifetime high precision measurements and magnetic muon studies will allow many parameters of the SM to be determined with unprecedented precision [31].

2.1.2 Facility design

As the neutrino beams at a Neutrino Factory will be produced from the decay of muons circulating in a storage ring, the primary aim of the accelerator complex is to store as high a muon intensity as possible. The muon production starts

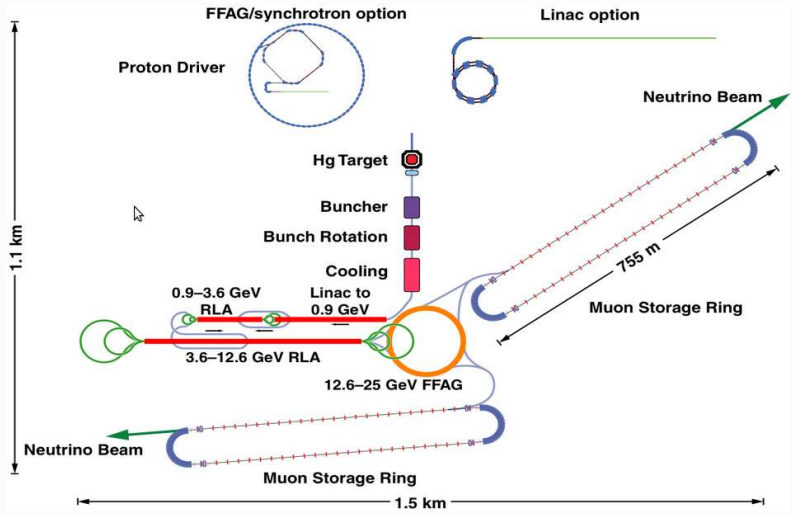

Figure 2.2: Schematic layout of the Neutrino Factory.

with a high power proton source to create intense bunches of protons which are fired into a target. The pions created in the collision are subsequently captured and transported along a decay channel, where they decay to muons. The resulting muon beam will have a large size and a large spread in longitudinal and transverse momentum, i.e. a large emittance, which must be reduced to avoid a large fraction of the muons being lost during acceleration and subsequent injection into the storage ring. The reduction of the momentum spread and transverse emittance takes place in two stages, called respectively rotation and cooling. The muons are then accelerated to a final working energy in a series of accelerators, before being injected into the storage ring.

A number of different designs exist for the Neutrino Factory [40]. Although there are substantial differences between them, each design consists of the same basic components. Fig. 2.2 shows how these components are laid out in the CERN design. A proton driver produces the very high proton-beam-power (4 MW) necessary to achieve the neutrino intensity required for the neutrino oscillation studies. To minimize the longitudinal emittance of the initial muon beam, the proton bunches must be no more than a few nanoseconds long. Due to the high beam-power and small size, the power density in the target far exceeds that of any comparable facility. Building a target that can withstand the mechanical and thermal stresses that such a beam will create is a major challenge and is the subject of an active R&D program. The pions are then captured and focused by a powerful magnet.

Once captured, the pions decay to produce muons in a decay channel that is $30-40$ m long. The large momentum spread of the decay muons will be reduced using phase rotation in which early (high energy) particles are de-accelerated and late (low energy) particles are accelerated using, for example, a system of RF cavities. The muons can then be captured into RF bunches, and the transverse emittance reduced using an ionization cooling channel. Ionization cooling is discussed in detail in section 2.2.

2.2 Ionization cooling

Cooling the high emittance muon beam produced at the end of pion decay pipe in the Neutrino Factory is a essential step to achieve the high intensity, monochromatic and well collimated beam necessary for the completion of its physics goals. Four beam cooling techniques exist nowadays and have been studied in the past [41]:

- the **radiation cooling** takes advantage of the natural phenomenon of synchrotron radiation emitted by all relativistic charged particles accelerated or stored in a ring;
- the **electron cooling** consists in the injection of a well collimated electron beam in parallel of the primary beam (typically a heavy ion beam). The cooling is achieved through the multiple Coulomb collisions between the two beams.
- the **stochastic cooling** is based on an active feedback system that reduces the beam emittance by correcting the motion of the particles, e.g. by tuning the surrounding magnetic field;
- the **ionization cooling** simply uses the energy loss produced by the passage of charged particles through a relatively dense medium.

The first three methods are sound and have proved their value in e^+e^- synchrotrons and hadron colliders but have never been applied to the cooling of muons. In fact, the mass of the muon ($\sim$ 200 times the electron mass) makes cooling by radiation damping impossible while its short lifetime excludes the use of either the second or the third option. Ionization cooling however, given the long interaction length of muons, can be adopted to cool muon beams.

A conceptual representation of angular spread reduction through ionization cooling is provided in fig. 2.3. The muon energy loss in the absorber per unit of distance is described by the relativistic Bethe formula [42]. The muon loses momentum both in the transverse and longitudinal frame but only the longitudinal component is restored by re-accelerating the beam.

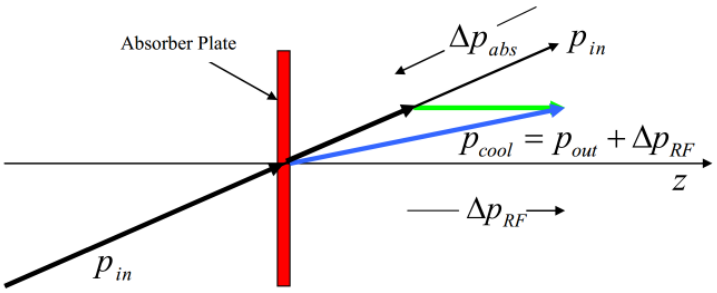

Figure 2.3: Conceptual picture of the principle of ionization cooling [43]. Each particle loses momentum by ionizing an absorber, but only the longitudinal momentum is restored by RF cavities.

While multiple ionization of the absorber contributes to cooling the beam, Coulomb scattering, on the other hand, acts as a heating factor. As a result, the

cooling effect dominates for low Z absorbers [41] combined with strong focusing fields.

The main parameter used to quantify the cooling is the emittance ϵ, defined as the volume occupied by the beam in the phase space. It can be expressed as $\epsilon = \sqrt{D}$, where D is the determinant of the 6-dimensional covariance matrix of the beam particles in the 6D coordinate system $(x, y, t, dx/dz, dy/dz, cdt/dz)$ with z the beam direction. Taking into account the natural decrease of the beam size with the acceleration as well, it is convenient to define the normalized emittance ϵ_n as a function of $(x, y, t, p/mc \cdot dx/dt, p/mc \cdot dy/dt, p/m \cdot dt/dz)$.

The transverse emittance is defined as the emittance in one of the 2D plane $(x, dx/dz)$; in a solenoid channel, the cylindrical symmetry argues for this to be calculated as the square-root of the transverse 4D emittance. In 2D, the covariance matrix is greatly simplified and the squared transverse emittance along the x reads

$$\epsilon_x^2 = D = \det \begin{pmatrix} < x^2 > & < x\theta > \\ < \theta x > & < \theta^2 > \end{pmatrix} =< x^2 >< \theta^2 > - < x\theta >^2, \tag{2.1}$$

with θ the angular divergence of the particle in the x-z plane. Following the process described thoroughly in [44], i.e. normalizing the emittance, introducing the muon Bethe function dE_μ/dz as the main cooling factor, neglecting the correlation and the growth of the beam size, defining the transverse beam beta function[2] $\beta_\perp$ and introducing the Moliere scattering formula, we get:

$$\frac{d\epsilon_{xN}}{dz} \simeq -\frac{1}{\beta^2}\frac{\epsilon_{xN}}{E_\mu}\left|\frac{dE_\mu}{dz}\right| + \frac{1}{\beta^3}\frac{\beta_\perp}{2}\frac{E_S^2}{E_\mu m_\mu c^2}\frac{1}{X_0} \tag{2.2}$$

as the expression of the normalized transverse emittance. $E_S = 0.014$ GeV a constant and X_0 the muon radiation length. The first term is a cooling factor, i.e. reduces the beam emittance (negative sign) while the second one is the Coulomb heating factor. The longitudinal emittance is defined similarly in the time-energy dimensions.

To minimize the heating term, which is proportional to $\beta_\perp$ and inversely proportional to the radiation length, the best option is to use pressurized liquid hydrogen as the energy absorbing medium, with $dE_\mu/dz = 30$ MeV/m and $X_0 = 8.7$ m, and to use superconducting solenoid focusing to give a small value of $\beta_\perp \sim 10$ cm, rather than quadrupoles; this corresponds to large beam divergence at the location of the absorbers, so that scattering in the absorbers gives a relatively small contribution to the emittance.

An additional technical requirement is high-gradient re-acceleration of the muons between absorbers to replace the lost energy, so that the ionization-cooling process can be repeated many times. The achievable RF gradient determines how much cooling is practical before an appreciable fraction of the muons have decayed or drifted out of the bucket.

2.3 MICE cooling channel

The International Muon Ionization Cooling Experiment (MICE [29]) is an R&D project whose main goals are to study the feasibility of a Neutrino Factory based

[2] The beta function describes a particle moving in an accelerator and provides an emittance-independent representation of the properties of a beam transport system, i.e. $< x^2 >= \beta_\perp \epsilon_x$.

on a muon storage ring and the experimental demonstration of the ionization cooling technique.

The experiment is currently under construction at the Rutherford Appleton Laboratory (RAL) in the UK. The already existing ISIS synchrotron is used as a 800 MeV proton driver to create a pion beam that further decays into the muons required in the cooling channel. A titanium target is dipped into the ISIS beam every second, producing a pion beam in the first section of the MICE experiment. The pions are captures and collimated by a triplet of quadrupoles (Q1-Q3), a dipole (D1) and are left to decay in a 5 m decay solenoid (DS). The muons are subsequently identified by a scintillating fibre monitor (GVA1) and pass through another dipole and a triplet of quadrupoles (D2+Q4-Q6) before entering the cooling channel. A layout of the beamline is shown in fig. 2.4 (a).

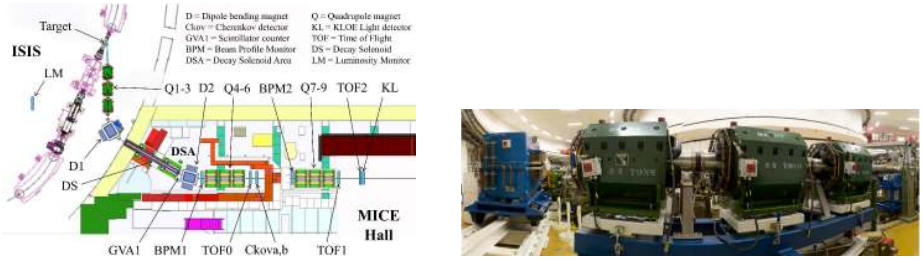

(a) (b)

Figure 2.4: (a) MICE layout in the experimental hall: the main components needed for the muon transport are shown. (b) A photo of the first triplet of quadrupole and first dipole magnets (Q1-Q3+DS1) that capture and select the momentum of the pions produced in at the interaction point.

MICE will typically work with a muon beam with a momentum in the range $140 - 240$ MeV/c, $\beta = 42$ cm at the centre of the absorber and normalized emittance[3] between $1 - 10\pi$ mm·rad [29]. The cooling section design follows the guidelines of the US Feasibility Study-II [33]. A schematic layout (not in scale) of the detectors and cooling section elements position is shown in fig. 2.5.

The basic elements of the MICE cooling channel are three Absorber and Focusing Coil (AFCs), and the two RF cavity and Coupling Coil (RFCCs) stations [46]. The overall length of the channel is ~ 5.5 m. Each AFC module contains a liquid hydrogen absorber at a cryogenic temperature that provides the energy loss of muons, and a pair of focusing coils to reduce the beta function that ensures a small equilibrium emittance. Each RFCC station consists of four 201 MHz normal-conducting RF cavities and one super-conducting solenoid.

The tracking and particle identification is accomplished by two scintillating fibre detectors and Time Of Flight+Cherenkov systems. The upstream PID detectors provide the background reduction from pions and electrons while the downstream ones, together with a dedicated calorimetry station, give the electron rejection at the end of the channel. The overall length of the MICE experiment is ~ 11.5 m [29].

Three TOF stations [47] are positioned along the cooling section to provide the time coordinate (t) measurement for the emittance estimation. TOF0 is

[3]The upstream emittance can be tuned by a set of diffusers at the entrance of the cooling channel [45].

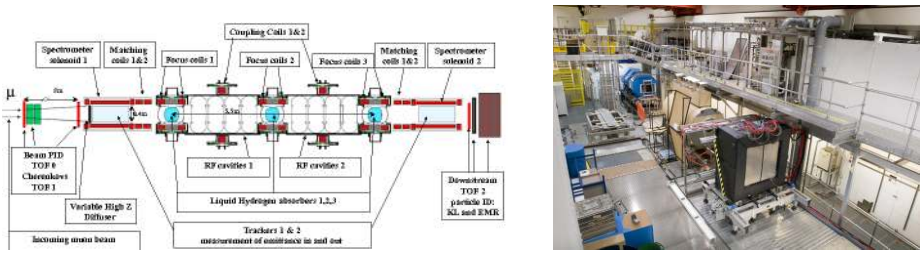

(a) (b)

Figure 2.5: (a) schematic layout of the MICE cooling channel (with the beam entering from the left [29]. (b) A photo of the MICE experimental area in October 2013: the last triplet of blue dipoles (Q7-Q9), TOF1 (at the end of the triplet), a dummy of SS1 and the EMR can be seen in the picture.

placed at the beginning of the channel, while TOF1 and TOF2 are positioned respectively at the entrance and at the exit. The main task of the upstream TOFs is the pion background separation at low momenta (below ~ 210 MeV/c); they also supply the trigger for the experiment in coincidence with the ISIS clock [29]. TOF2 at the end of the section selects the particles passing through it for the downstream emittance measurement and the cooling efficiency estimation. The TOF stations have a common design: two planes of fast scintillator counters are organized in a X-Y configuration.

Given that for a momentum range between 220 and 360 MeV/c the time of flight difference between muons and pions is ~ 2 ns over a distance of ~ 10 m, two Cherenkov counters are used to provide a sufficiently good pion/muon separation [48]. The active radiator is a high density silica aerogel plate while the produced light is readout by four 8 EMI 9356 KA photomultipliers. The association of the CKOV and the two first TOF station allows to achieve a beam purity of up to 99.98% [49].

Charged-particle tracking in MICE is provided by two solenoidal spectrometers [50] that are required to determine the expected relative change in transverse emittance of approximately 10% with a precision of 1% (i.e. a 0.1% precision on the absolute emittance [29]). Each spectrometer consists of a 4 T superconducting solenoid instrumented with a 1.1 m long tracker, composed of five planar scintillating fibre stations. One of the trackers has been tested at RAL with cosmic rays: a spatial resolution of 682 ± 1 μm and an efficiency of $99.82 \pm 0.1\%$ have been found [50].

The electron background rejection at the end of the cooling channel is based on the Electron Muon calorimeter (EMcal) station: the electron shower starts in an electromagnetic preshower calorimeter (KLOE-Light) while the penetrating muons are detected afterwards in a fully active scintillating bar tracker-calorimeter (Electron Muon Ranger, see next chapter for a detailed description). The KL consists of a 80×80 cm^2 grooved lead layer transversally segmented with 1 mm diameter blue scintillating fibres inserted and glued in the lead holes. The thickness is ~ 4 cm corresponding to less than 2.5 radiation lengths. The KL relative energy resolution has been found to be $\sigma_E/E = 7\%/\sqrt{E(\text{GeV})}$ while the time resolution is $\sigma_t = 70$ ps$/\sqrt{E(\text{GeV})}$ [51].

3 Electron Muon Ranger

The particle identification upstream the cooling channel in MICE is provided by the Time of Flight detectors (TOF) [47], the Cherenkov detector (CKOV) [48] and the trackers [50]. Nevertheless, simulations [52] have shown that TOF2 can't ensure alone the measurement of the downstream beam emittance. A detector able to accurately discriminate the electrons from the muons is required to achieve the commissioned level of precision [29].

More specifically, a tracker-calorimeter is necessary for the particle identification at the end of the MICE channel. This detector consists of a calorimeter (KL) [51] coupled to a Fully Active Scintillator Detector, the Electron Muon Ranger (EMR), which characterization is the centre of interest of this master thesis.

In this section, we will focus on the the description of the EMR and its critical role in MICE. The detector is based on triangular scintillating bars that add up to almost 1.5 tons of plastic while the electronics chain relies on dedicated Front End Boards (FEB), Digital Buffer Boards (DBB) and standard VME modules. Several characterization tests have been performed in the context of this thesis. Some of them were conducted during the building process (fibre luminosity and MAPMT readout) while the rest of the lot were done on the entire machine.

The detector is currently fully operational and located in the MICE channel at RAL. The EMR will however undergo minor updates in the months to come as its ageing Philips PMTs [53] will be replaced by brand new Hamamatsu PMTs and many DAQ parameters will be optimized.

3.1 Purpose

Particle identification upstream and downstream the cooling channel is a fundamental task to achieve the required precision on the beam emittance measurement [29]. As its name would suggest, MICE works with muon beams of tunable emittance and energy. As a result, everything which is not a muon is considered background. There are three main sources of background in MICE:

- some of the pions, from which the muons are produced, that remain in the beam (the beam transport line before the cooling section ensures a muon purity better than 99.9% [54]);
- the dark current originating from the RF cavities operating in high electric and magnetic fields. Electrons can be ripped off the surface of the cavities and accelerated along the cooling channel causing bremsstrahlung photon emission. In turn this corresponds to a source of background in the trackers [52];
- muons decay inside the cooling section or in one of the spectrometers. The number of muons and electrons arriving at the end of the cooling channel as a function of the muon initial momentum at Q9 [29] is given in fig. 3.1. At low energies, the great part of the muons in the beam decays into electrons and some of the background is due to muons decaying at rest.

The separation of pions from muons and the RF electron background rejection at the beginning of the cooling section are provided by the upstream TOFs,

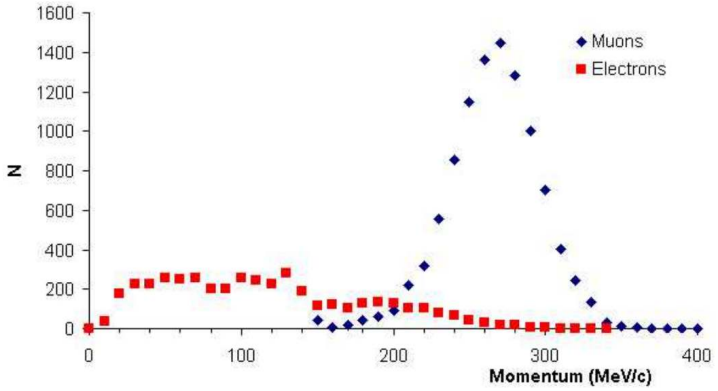

Figure 3.1: Momentum distributions of muons and electrons arriving downstream of the second spectrometer [29]. The lower the energy, the larger is the fraction of muons that decay along the cooling channel.

the CKOV station and the spectrometer trackers [52]. The main concern for the emittance high precision measurement is thus represented by the downstream particle identification. Kinematics cuts can reject about 80 % of decay electrons [29], but this is not enough to avoid a lack of accuracy in the beam emittance measurement. Dedicated detectors are thus necessary to separate electrons from muons.

Several solutions based on a calorimeter system have been proposed and their performances in terms of electron/muon separation efficiency have been studied with G4MICE simulations [52]. Fig. 3.2 shows the results for three alternative designs. The red line indicates the configuration in which four KL-like layers are present, the black one shows a design that foresees the use of a front KL layer followed by a fully active plastic scintillator detector (KL+SW[4]) while the purple line represents a solution with only the TOF2. The obvious choice is the second one [52].

The basic idea for the downstream background rejection is to distinguish electrons from muons using the longitudinal profile of the electromagnetic shower at the end of the cooling section [52]. A high Z material (e.g. a lead preshower) combined with a low Z one (e.g. scintillating plastic) is the ideal choice: the electrons lose most of their energy in the preshower generating an electromagnetic cascade in the following layer while the muons penetrate the high Z material without interacting. This means muon events can be distinguished from the background ones thanks to their different topology [52].

[4]The original proposed design of EMR, called SandWich (SW), was exploiting a KL-like front layer followed by 10 modules of plastic scintillator with different thicknesses [52]. The detector design has been subsequently changed basically because of cost reduction and simplification in the manufacturing.

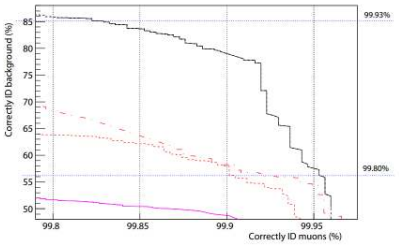

(a)

Initial mom.	No cal., with TOF	KL, no TOF	SW, no TOF	KL, with TOF	SW, with TOF
140 14 MeV/c	47.8%	56.2%	79.5%	58.2%	79.5%
170 17 MeV/c	54.1%	48.8%	56.4%	59.0%	67.8%
200 20 MeV/c	59.0%	57.3%	74.2%	79.4%	87.6%
240 24 MeV/c	64.5%	65.0%	91.4%	80.0%	92.2%
TURTLE				83.5%	

Not meeting req. Meeting basic req. Meeting safety req.

(b)

Figure 3.2: (a) The PID performance, $p_z^{TOF1} = 140 \pm 14$ MeV/c [52]. The solid black line indicates the performance using SW, while the dash-dotted red line is the performance using only KL. The dashed red and black lines are the performance using KL and SW without TOF information respectively, and the purple solid line is the performance when no calorimeter is used. (b) The numbers correspond to how much of the background is rejected at 99.9% signal efficiency [52]. Slide from presentation by Rikard Sandström at MICE collaboration meeting 2006 in Osaka.

3.2 Design

In fig. 3.3, we can see a 3D engineering rendering of the Electron Muon Ranger (EMR) and a picture of the detector in MICE hall. EMR consists of 48 layers, organized in an X-Y geometry (24 modules, a module corresponding to 1X+1Y planes), of extruded scintillator bars [55] made of blue-emitting DOW Styron 663 W polystyrene + 1% PPO + 0.03% POPOP dopants[5]. The layers are positioned one after the other and are supported by a metallic frame. The whole detector is enclosed in a black aluminium box (EMR Outer Box, EOB) to shield it from the ambient light.

Each layer consists of 59 bars with a triangular shape (base=3.3 cm and height=1.7 cm) and 1.1 m long, for a total of 2832 bars for the whole detector. A complete EMR module covers an active region of ~ 1 m^2 . As a layer weighs $\sim$ 28 kg, that means that the whole scintillating volume flirts with the $\sim$ 1.5 tons mark.

The light yielded by each bar is conducted by one 1.2 mm BFC-91A Wave Length Shifter (WLS) fibre [56]. Each fibre goes through the whole bar and ends on both side by a polished section. A connector is screwed onto the end sections, to which a clear 1.5 mm polystyrene fibre [57] can be connected. The clear fibres connectors are simply clipped against the polished end of the WLS fibres and have a variable length depending on the distance between their end point and the photomultiplier [58]. To protect the fibres and support the photomultipliers and their electronics, each layer is equipped with an aluminium box on each side that also provides light tightness. Fig. 3.4 summarizes the light transport process.

The clear fibres are connected on both sides to two different photomultiplier systems. On one side, the fibres exiting from each bar are grouped together and are connected, through a dedicated mask, to the single anode Philips XP 2972

[5]PPO (2,5-Diphenyloxazole) and POPOP (1,4-bis(5-phenyloxazol-2-yl) benzene) are scintillators. POPOP is used as a wavelength shifter; its output spectrum peaks at 410 nm.

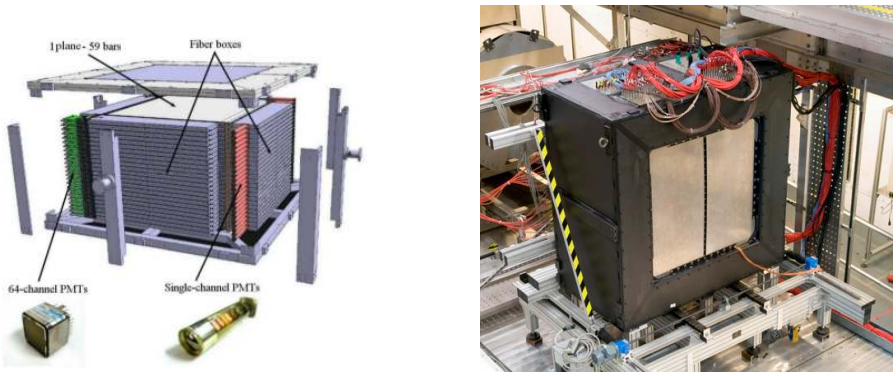

(a) (b)

Figure 3.3: (a) A 3D engineering view of the EMR detector and its mechanical support. The placement of the SAPMTs, MAPMTs, FEBs and fibre boxes are represented [59]. (b) Picture of the EMR box placed in the beamline of MICE for Step I.

PMT (SAPMT) [53], which purpose is to measure the total charge deposited in one plane, i.e. the energy loss. The front end electronics of the PMT has been adapted to put it directly inside the metallic support that provides the shielding against the magnetic field (mu metal). Each SAPMT is powered by a 1800 V high voltage power supply and connected analogically to a VME Readout Board (VRB).

On the other side, the clear fibre coming from each bar is fitted, through a dedicated square mask, against one specific channel of a multianode green enhanced PMT (MAPMT) R7600-00-M64 (H7546B assembly, Hamamatsu [60]). The rear of the MAPMT is soldered to a 4 layer rigid-flex (kapton) circuit that allows the needed mechanical flexibility. Each MAPMT is powered by a 700 V high voltage power supply and connected to a Front end board for further processing.

The EMR electronics chain has to cope with the MICE experimental duty cycle which consists in a 1 ms spill every second. Within this spill, up to one good event every 5 μs has to be recorded. In this time scale, the EMR electronics chain has to sample and discriminate the signals of each MAPMT, assign a time stamp to every bar over threshold, store data in a digital form and make them available for the readout at the end of the spill.

The EMR electronics is divided in 3 main blocks:

- the Front End Boards (FEBs), which are located near the fibres exit. They provide the connection to the MAPMT, the ASIC for the MAPMT signals conditioning and the interface with the second block of the electronics;
- the Digital Buffer Boards (DBBs), which are data storage modules coupled to each FEB. they are the boards that sample the digital outputs of the ASIC with a 400 MHz clock and, in presence of a particle trigger, store the above threshold bar numbers with a timestamp and a Time over Threshold measurement to send them to the DAQ system in the interspill period.

  The digital outputs are the ASIC outputs; the signal from the MAPMT

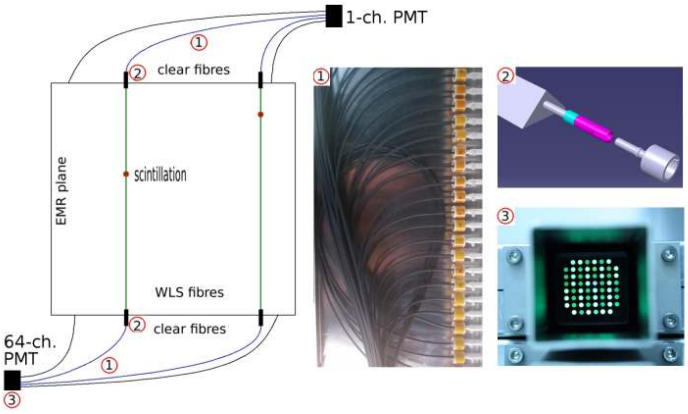

Figure 3.4: Scheme of the light transport in a plane of the EMR. After scintillation, light is transported by the WLS fibre to the connectors on each end of the bar (2). It is then transmitted through the clear fibres (1) to finally reach the fibre mask (3) that is fitted against the PMT. The mask represented in this figure is the MAPMT fibre mask. [58, 57]

is shaped, the Time over Threshold is measured and digitized. The choice to use only the digital information (time in ADC counts) is a direct consequence of the beam structure as integrating the charge for each channel would take too long. The sampled data are stored with a timestamp and the trigger number in the spill for the offline reconstruction of the event;

- the Data AcQuisition system (DAQ), consisting in a VME crate hosting the Configuration Boards (VCBs), the Readout Boards (VRBs) and the flash Analogue-to-Digital Converters (fADCs). The VCB main task is to flash the FEBs' firmware that is the setting of the ASIC mask (e.g. pre-amplifier gain, shaper parameters or discriminators threshold). The configuration of the DBBs (in terms of clock rate, data format, etc.) is also managed by this board. The boards are configured at the beginning of each run. The MICE particle trigger is sent to the detector and the readout boards straight from the control room through a NIM shaper. The clock synchronization between the boards is performed using the trigger signal.

A schematic representation of the complete electronics chain is shown in fig. 3.5. The analogue signal of each single channel PMT is sampled and digitized by a V1731 Wave Form Digitizer (WFD, CAEN [61]) housed in the VME crate.

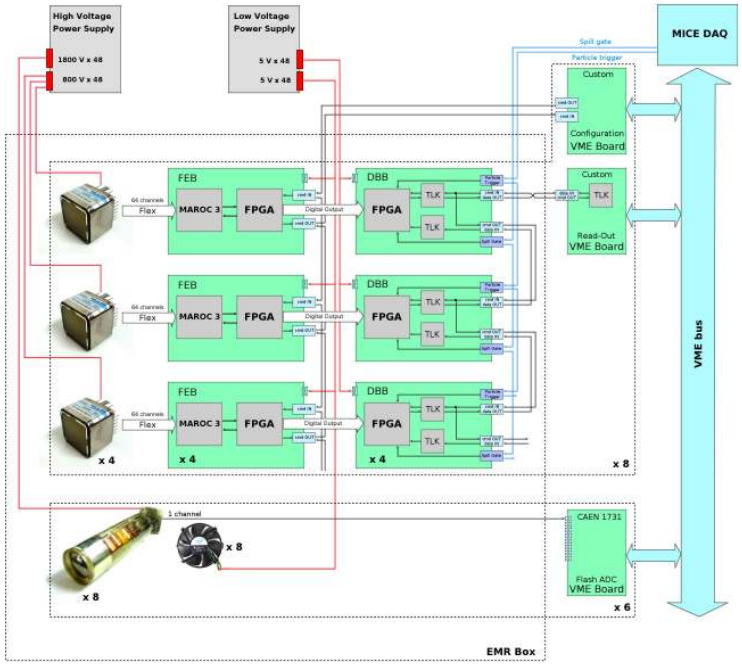

Figure 3.5: Scheme of the electronics chain for the readout and setting of the EMR detector. The SAPMTs are currently connected to fADCs housed in the VME crate. The MAPMTs signals are sampled and digitized by the Front End Boards (FEBs) and the Digital Buffer Board (DBBs).

3.3 Software

The EMR raw data is structured as shown in fig. 3.6 and consists in an array of subcategories. Each run is divided in a collection of raw ROOT files containing around 50 MICE spills. A spill contain the data arrays for all the active detectors in the cooling channel at the time of data acquisition.

In the raw data, if we take a closer look at the EMR section, for each particle trigger ($\sim$ 50 per spill with no DS during Step I), we have an array of planes that have been hit by the particle. The plane hit contains the information on the total integrated charge for this trigger and the number of bars hit in the plane. Each bar within the plane holds the Time over Threshold measurements and the timestamps for all the hits that were recorded in it.

The EMR reconstruction will be useful in the signal acquisition efficiency analysis section. Its process is still under refinement but is already fully functional and divided in the following steps:

- the bar hits are sorted according to the delay between their timestamp t_hit and the trigger (pair of slabs hit in TOF1) time t_trig, i.e. $\Delta_t = t_hit - t_trig$. If the hit is close to the trigger, we consider that the hit corresponds to the primary particle trail and is stored in the first hit array. If the hit happens short after the primary time interval, it is associated with electronic noise and is stored in a second array. Finally, if the time doesn't correspond to a trigger, it is moved to a third array which will contain the decay products

hits as well as random noise;

- for each hit in a given plane , the missing coordinate is reconstructed as the average of the two adjacent planes. In the case of the X plane, the Y coordinate is the average of the position of the hits in the adjacent Y planes;
- the hits in the third array are associated in bunches according to their time stamp. The track of the primary and secondary tracks are fitted in both projection using the simplistic algorithm described above. Finally, the software tries to associate piecewise each bunch to one of the primary track within the spill by geometrically matching the end point of the primary track with the beginning of the secondary one.

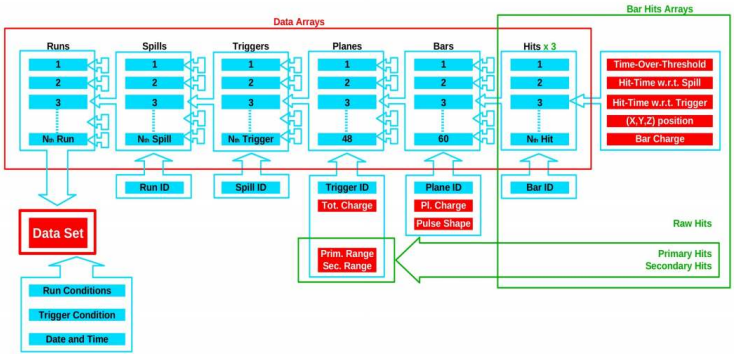

Figure 3.6: Data structure of the EMR. Each subsection contains its own set of variables. Some of them are defined during data acquisition such as the total plane charge of the bar Time over Threshold measurement but most of them are filled during reconstruction, e.g. the particle range or the bar charge.

4 MAPMT readouts

4.1 Experimental set-up

To test the readout electronics before shipping the EMR to RAL, a test bench was developed using an LED driver instead of implementing them into the EMR first. This set-up provides a steady light pulser which intensity can be kept unchanged from one readout chain to another.

A schematics of the EMR readout electronics is represented in fig. 3.5. The light coming from the LED pulser shines on all the channels of the MAPMT. These primary signals are shaped and digitized by the FEB and DBB before being sent to a VME readout board (VRB). A VME configuration board (VCB) is used flash the firmware or modify the readout of the parameters of the tested FEB.

A Time over Threshold (ToT) measurement was recorded in each channel of the MAPMT for 10^6 LED pulses. This measurement is obtained by shaping the MAMPT primary signal, setting an arbitrary threshold and recording how long the signal stays over this given value. It is output in ADC counts (1 ADC Count = 2.5 ns).

4.2 Results

The distribution of Time over Threshold is plotted for each channel of plane 1 in fig. 4.1. We can clearly see in this case that none of the channels are flawed, they all record similar signals and thus have the same distributions. The most numerous are the very high energy hits corresponding to the primary LED signal while the low ToT band corresponds to the trailing noise of each signal. The arched behaviour that can be observed on the right side of the plot every 7 or 8 bars is explained by the MAPMT mask structure. Each bunch corresponds to a distinct row of the MAPMT mask; the channels at the edges of these arches are in fact on the outside of the mask and in consequence receive a little less light and are not cross-talked to (see section 7).

An example of a malfunctioning readout chain is given in fig. 4.2. In this plot, two channels are obviously dead as they don't record a single hit. The others are clearly not working properly as the distribution does not peak where it is expected. The tremendous amount of low energy hits suggest an unacceptable level of noise. FEBs presenting this type of behaviour are rejected from the pool and another board is used. At the end of the testing, all the FEB integrated in the EMR are functioning properly. An exhaustive set of Time over Threshold distributions is given for each plane in [62].

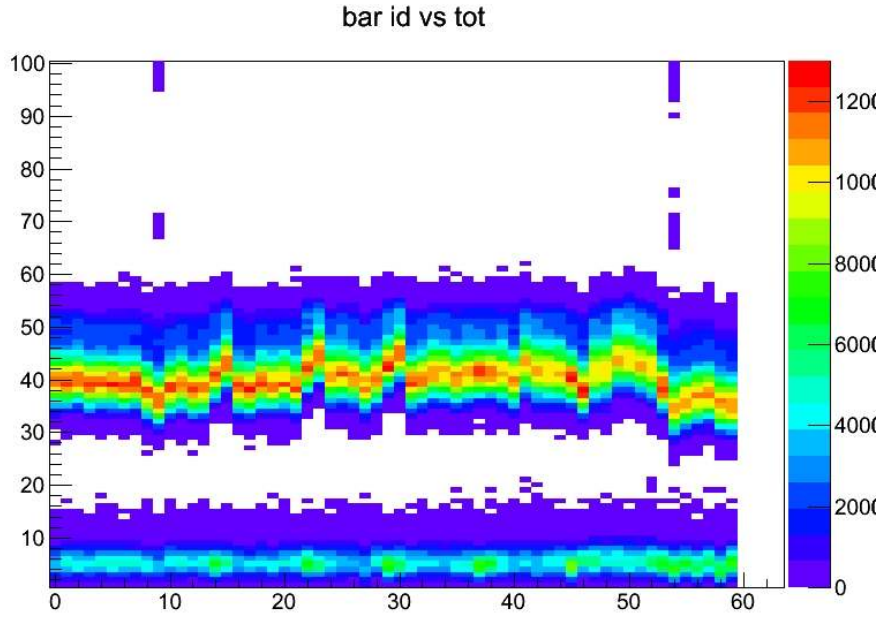

Figure 4.1: Time over threshold distribution of a functional readout chain. Each channel responds normally and gives a ToT distribution similar to the others.

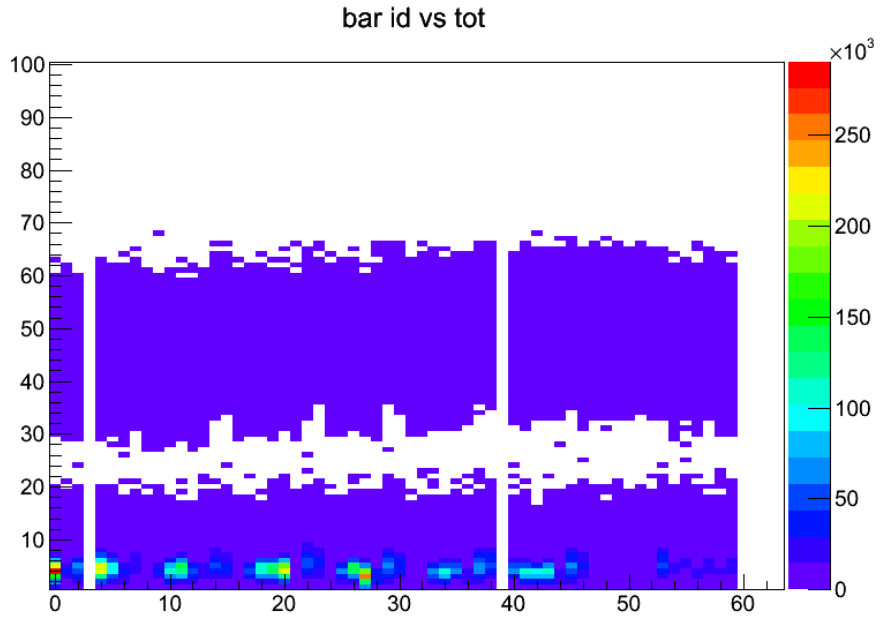

Figure 4.2: Time over threshold distribution of a malfunctioning readout chain. Two channels are clearly dead as they don't record any signal while the others record a lot of low ToT hits, i.e. noise.

5 Clear fibre luminosity

5.1 Experimental set-up

To measure the luminosity of each fibre with respect to the others, a Canon® EOS 1000D camera is used as primary measuring tool. Each time a plane is completely assembled, the camera is placed right in front of the fibre bundle mask that is to be coupled with an MAPMT. The camera is placed at a constant distance off the bundle and the following settings are kept unchanged:

- exposure = 0.05 s;
- aperture value = 5.00 EV (f/5.7);
- no flash.

A black light-proof heavy duty fabric cover is lowered over the whole detector so that the measurement is not influenced by the ambient luminosity. LED light sources are placed on the top part of the cover and shine directly on the 59 topmost bars of the EMR. When everything is in place, a picture of the fibre bundle mask is taken. Finally, the picture is layered with a grid as depicted in fig. 5.1 and the luminosity in each compartment is computed from the amount of photons recorded in that region of the CMOS sensor.

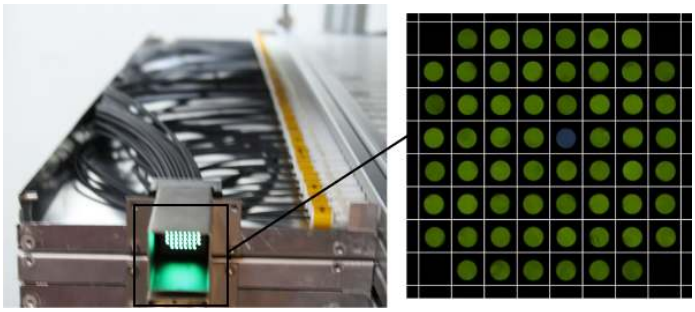

Figure 5.1: Close up picture of a fibre bundle mask layered with grid allowing to compute the luminosity of each fibre.

5.2 Results

The measured luminosity is averaged for each plane and a deviation in percent from this average is computed for each bar, i.e. the relative deviation of channel i, reads

$$\frac{\Delta L_i}{\overline{L}} = \frac{1}{\overline{L}}(L_i - \overline{L}). \tag{5.1}$$

with $\overline{L} = \frac{1}{59}\sum_{i=1} 59 L_i$, the average luminosity in a given plane. The deviation is plotted as function of the channel ID for plane 1 in fig. 5.2. The rightmost entry corresponds to channel 0 and is to be ignored as it corresponds to the test channel that wasn't lit when the picture was taken in plane 1.

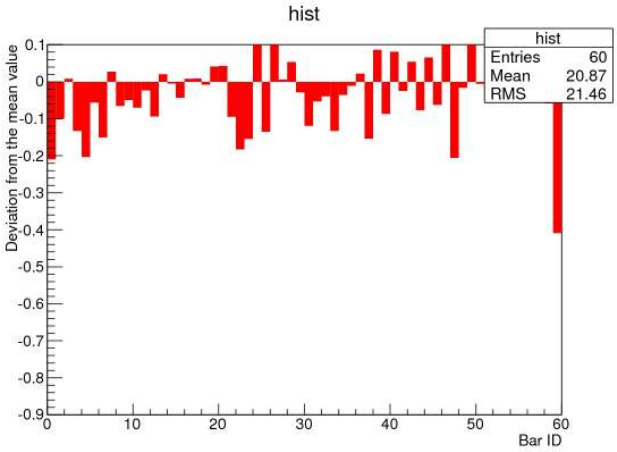

Figure 5.2: Deviation from the average luminosity $\Delta L_i/\overline{L}$ in plane 1. Most of the values are contained within 20 % of the average. The last bin corresponds to the test channel and wasn't lit at the time of data acquisition.

The distribution of deviations for all the planes and the 2832 bars is given in fig. 5.3. Only 2 fibres that are more than 40 % under the average luminosity in their respective plane and could be damaged. For the rest of them, the value is acceptable and, although calibration will be necessary, this won't influence the range reconstruction in the EMR as hits won't be lost because this deviation. An exhaustive set of luminosity plots is provided for each plane in [62].

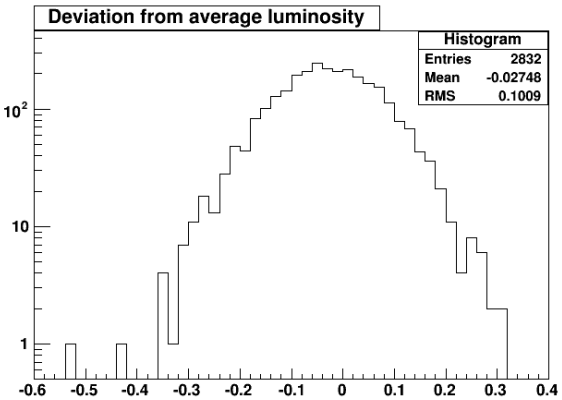

Deviation	Counts
$\Delta L/\overline{L} < -0.4$	2
$-0.4 < \Delta L/\overline{L} < -0.2$	130
$-0.2 < \Delta L/\overline{L} < 0.2$	2667
$0.2 < \Delta L/\overline{L}$	33
Total	2832

Figure 5.3: Distribution of the deviation from the average luminosity $\Delta L_i/\overline{L}$. Only two fibres are more than 40 % under and could be damaged.

6 Channel mismatch analysis

6.1 Potential causes

After the changes applied to the EMR design [58], a connector has been fitted between the WLS fibres glued inside the scintillating bars and the clear fibres going to the MAPMTs. As a result, a mismatch can occur if, during the building process, the technician in charge of connecting the fibres to the bars inadvertently connected a fibre to the wrong bar.

Moreover, in the manufacture of the fibre bundle itself, fibres could have been fitted in the wrong spot in the mask. Each fibre was manually tagged with a number ranging from 1 to 59 corresponding to each bar in the plane and thus is subjected to mislabelling.

Finally, a short circuit or other manufacturing problem in the FEB, DBB or VRB could result in an electronic mismatch and would cause artefacts in the detector as well.

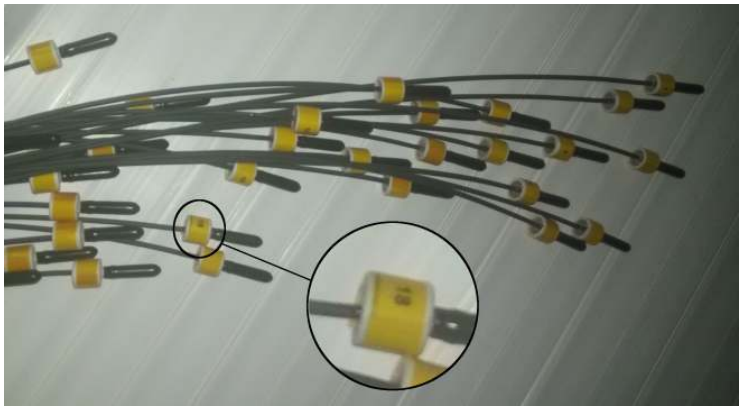

(a)

(b)

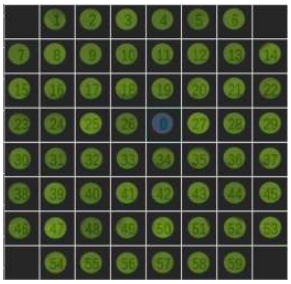

(c)

Figure 6.1: Channel mismatch hot spots: (a) clear fibre bundle magnified on one particular label that could be wrong; (b) connectors between the scintillating bars and the clear fibres, the connectors of two bars could be swapped; (c) clear fibre bundle mask, the fibres could be fitted in the wrong hole.

6.2 Data acquisition

To identify mismatched channels, it is necessary to use real tracks and to cover the whole detector with a lot of them to reach high statistical significance. That leaves us with beam data recorded in October 2013 for Step I or cosmic data. The former doesn't cover the whole detector as some of the muons and pions stop in it and the greater part of the beam is located in the centre of the EMR. As a result, cosmic data was used to perform this mismatch analysis. Cosmic muons are perfectly suited for this procedure as they always go through the detector without stopping and have no preferential location in the detector.

When the data sample used in this paper was recorded, the EMR was fully operational and was located in the MICE hall at RAL. The detector was positioned up right, planes vertical, perpendicular to the ISIS beam. Two pair of planes (15-16 or 31-32) were used as the particle triggers in coincidence with a spill gate of 3 ms generated by the DAQ program at a frequency as high as the DAQ process allowed it. In terms of logic language, it translates into $trigger = ((p15 \cap p16) \cup (p31 \cap p32)) \cap spillGate$ and is represented as a logic gate diagram in fig. 6.2.

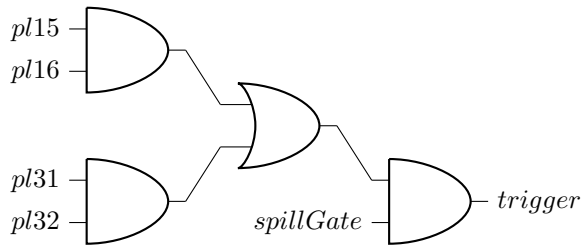

Figure 6.2: Trigger logic used to acquire cosmic data at RAL. The coincidence between one of two pair of planes and an artificial spill gate is used as the particle trigger, i.e. $trigger = ((p15 \cap p16) \cup (p31 \cap p32)) \cap spillGate$.

Data was taken for 60 hours and yielded around 223000 particle triggers. This corresponds to a trigger frequency of ∼1 Hz. The Time over Threshold (ToT) measurements were recorded along with their timestamps for the 2832 EMR channels for each trigger and are the only measurement used in this analysis. The integrated amount of hits recorded in each bar is represented in fig. 6.3. If we look closely at the distribution, we can see that no hits were recorded in a total of four bars. They are dead channels, namely bars 2, 3, 4 and 9 of plane 34. In each channel we recorded a number of hits N of order of magnitude $\sim 10^3$. As we will see later, the statistical significance of a mismatch goes as $\sqrt{N}$, so that we should reach an accuracy of order 1%.

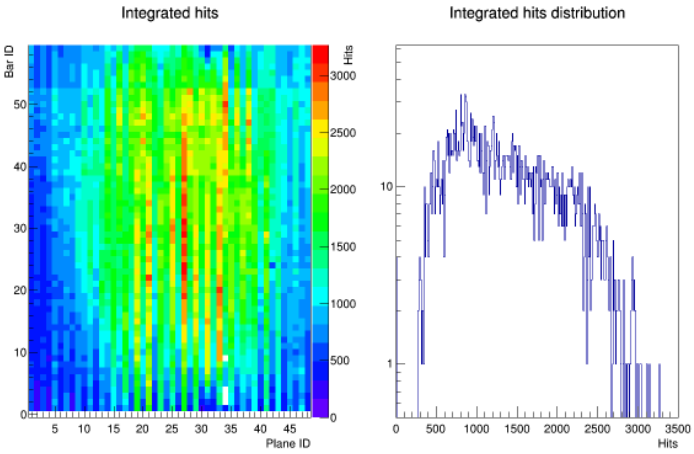

(a)

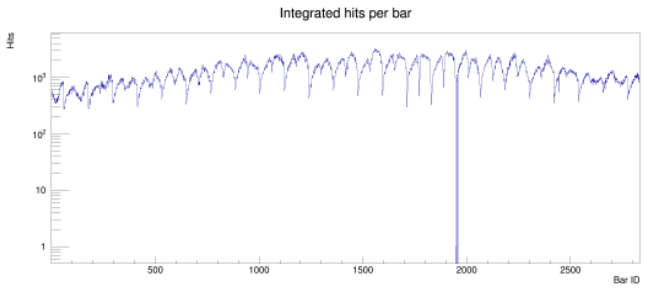

(b)

Figure 6.3: Integrated amount of hits recorded in order to probe eventual mismatched channels in the EMR. (a) Values given in each channel as a function of the plane ID and bar ID (left), distribution of the amount of hits (right). (b) Values given as a function of the channel ID.

6.3 Hit pre-selection

Channel mismatch is obviously not the only unwanted phenomenon occurring in our detector. One of the other subjects of this Master Thesis, the crosstalk, is another cause for hits where there shouldn't be any. In addition, electronic noise can be considered a signal and recorded along with physical hits. In consequence, two gross cuts are applied to every EMR event in order to clean the tracks as much as possible.

The first concerns the time elapsed between the trigger time and the hit time, i.e. $\Delta t = t_{hit} - t_{trig}$. There is always a delay before a bunch of hits generates a trigger and this delay is more or less constant. Restricting Δt to a small interval gets rid of most of the noise (noise distributed randomly or trailing a longer time after a trigger). The interval chosen is -94 ADC counts $< \Delta t <$ -80 ADC counts.

The second, the Time over Threshold measurement. If there is crosstalk,

not all the energy is transferred to the neighbouring channel, which means that most of the signals generated by this phenomenon will have lower intensity then the main one. For this reason, a cut was applied on the energy as well to focus on the primary hits generated by cosmic muons passing through the scintillating volume. The energy lower limit chosen is $ToT > 5$ ADC counts.

In fig. 6.4, the energy and time distribution has been combined in one 2D histogram. We can clearly see a peak at the typical MIP energy deposition ($ToT \simeq 15$ ADC counts) and typical Δt. The energy-time area used to reconstruct the tracks is limited by the red lines.

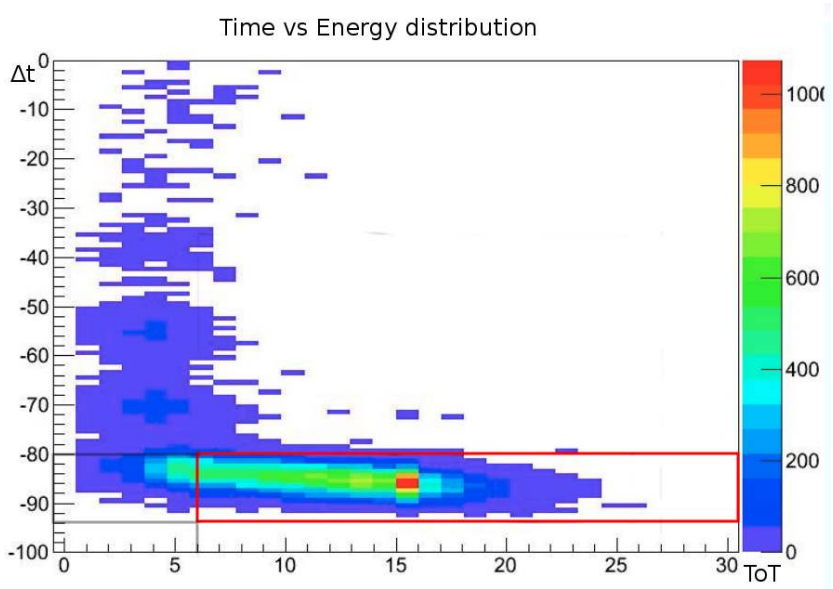

Figure 6.4: 2D histogram of the delay Δt vs the Time over Threshold distribution of the data sample used for the mismatch analysis. The red lines delimit an area of the eligible bar hits, the unit of both axis is ADC counts (2.5 ns).

This process is very important for the success of the fitting procedure described in the next subsection. Thanks to the hit pre-selection, the linear fits are generally more successful and the tracks are cleaner. The way this selection affects the tracks is shown in two single event displays below. They both represent the same event but the first one hasn't undergone any cuts while the second one has. For each display, the energy deposition and the timing is represented in the X planes on the one hand and in the Y planes on the other.

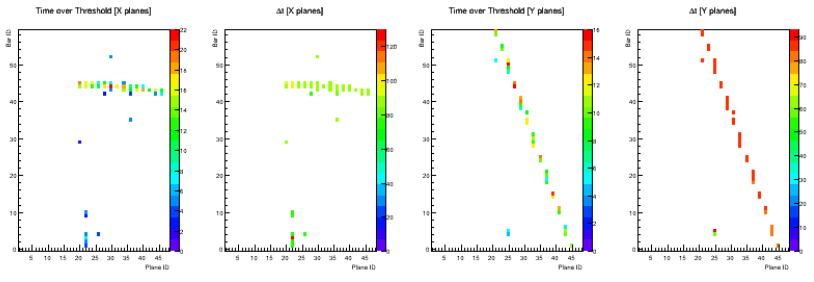

(a)

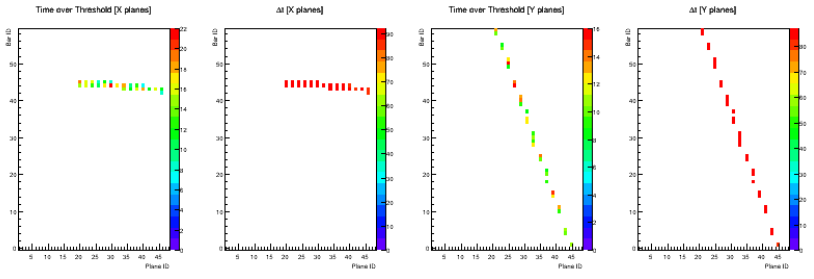

(b)

Figure 6.5: One event display of a cosmic muon going through the EMR, (a) before applying any cuts to the data, (b) after applying a selection on the timing and the Time over Threshold. The track is much cleaner after cuts.

6.4 Track reconstruction

To reconstruct the tracks and calculate the distance of each bar from the particle trail, it is necessary to fit each array of hits with straight lines. As a result, positions have to be attributed to every bar in the EMR.

In this context, triangular bars do not create the easiest geometry. We cannot choose the middle of a given bin to be the centre coordinates of the corresponding bar because it would not translate a triangle area repartition properly. To be accurate, one should consider the centre of mass of the triangle to be its middle point and linearly extend the error bars to its boundaries.

The section of the EMR bars are isosceles triangles. Their base measure 33 mm and their height 17 mm. In this analysis, the distances will be computed in terms of bin units and not MKS units. The reasoning behind this choice being that the distance we measure, in a mismatch analysis, should always average to a integer amount of bins. A bin unit *bu* is equal to 17 mm, i.e. the thickness of a plane. The height of a bar within a plane will subsequently be chosen to be exactly $2\,bu$. The bins are centred in the triangle COM which is located $1/3\,bu$ from its base and the error bars are prolonged from that point to the edges of the triangle. Fig. 6.6 represents the error bars and the measurements in *bu* of two adjacent bars.

This complicates the processing slightly because asymmetrical error bars have to be associated differently following the orientation of the bars, but it is much more relevant to the EMR design than to use square bins. The tracks

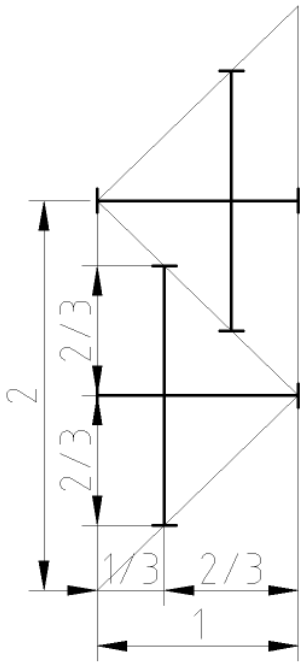

Figure 6.6: Asymmetric error bars in two adjacent scintillating bars. The middle point of the two crosses constitute de centre of mass of the scintillating bars while the bold lines constitute the uncertainty on this point. One bar is triangular shaped, has base of 2 bin units and a height of 1.

will still be displayed in plots with square bins but the calculation behind the distance measurement involves triangular ones. In this binning choice, y error bars overlap, which is what we would expect as so do the bars in the detector.

After assigning positions and uncertainties to all the bars hit, the track is fitted with a simple linear function of the form $f(x) = ax + b$. The X planes and Y planes are fitted separately as they represent two different projections of the three dimensional trail of a cosmic muon. The two fits are not combined into one because a mismatch only happens within the same plane, defying the purpose of 3D reconstruction. The fitting algorithm used is the least square method that involves a χ^2 measurement defined as

$$\chi^2 = \sum_i \frac{(y_i - (ax_i + b))^2}{\sigma^2}, \tag{6.1}$$

where x_i and y_i are the coordinates of a given bin centre and $\sigma = 2/3\,bu$ the uncertainty on the ordinate. In fig. 6.7, two successful fits of the same track are plotted in its X and Y projections. We can clearly see the influence that the choice of triangular bars has on the χ^2 calculation as most points are closer to the track than they would be if they were located at the centre of their respective square bins.

Finally, one more step is required to make the fit perfectly accurate. Sometimes, despite the pre-selection, a hit can be located far away from the track. It can be caused by high intensity crosstalk, synchronized noise or an actual

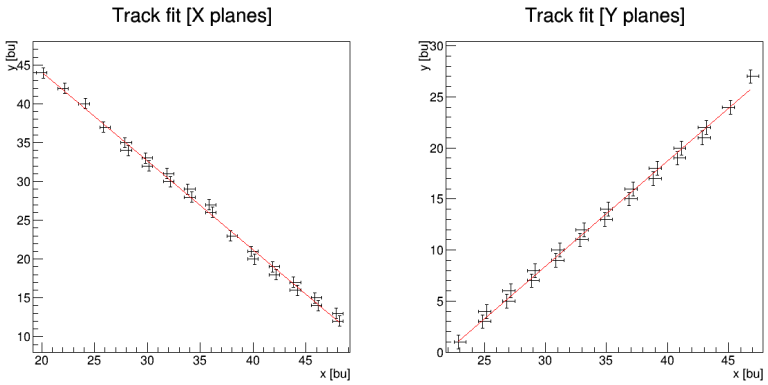

Figure 6.7: Successful fits of a cosmic muon track in the X and Y projections; the linear regression is represented in red. Most of the points are closer to track thanks to the triangular bin geometry adopted for this analysis.

mismatch. These hits can influence the location of the linear regression quite significantly and need to be excluded from the fitting procedure. In order to distinguish these hits from the main track, their distances from the primary fit is calculated for each one of them. This measurement Δs is represented by the green line in fig. 6.8 and, in terms of our variables, reads

$$\Delta s = \Delta y \sin(\theta) = \Delta y \sin(\mathrm{Atan}(a)), \tag{6.2}$$

with a the slope of the fitted line.

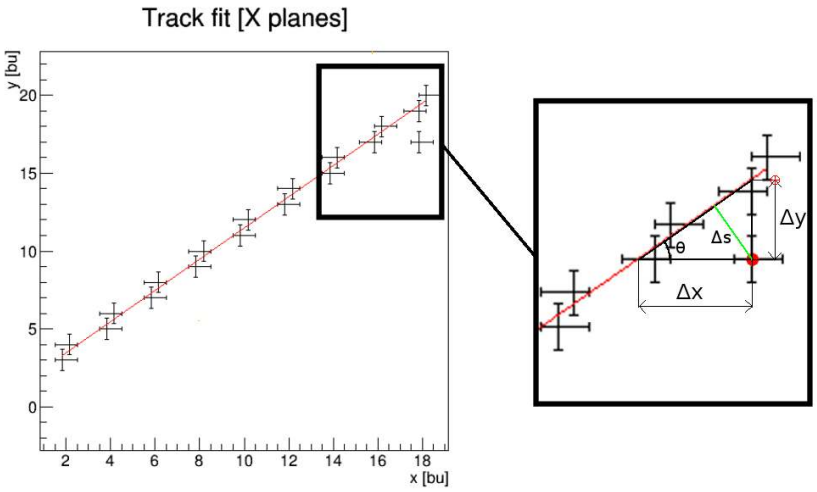

Figure 6.8: Illustration of the distance measured in the fitting process.

All the hits for which the distance calculated exceeds $2\,bu$ are rejected from the fitting sample but kept to be processed in the mismatch analysis. The graph is then fitted one more time, including only the hits located close to the track to achieve maximum accuracy.

6.5 Hit post-selection

Each hit recorded in the EMR which reached this stage still needs to undergo one last selection process before it's included in the analysis. There are three selection criteria that have to be fulfilled:

1. the track primary fit χ^2 value can't exceed 250. This prevents the very messy events such as electromagnetic showers from being included into an analysis requiring clean tracks;

2. the muon has to hit at least 10 planes for a given projection; this gives an extra criteria bounding the tracks to be more or less horizontal and not to be a dot in the EMR, which would make the position of the hits with respect to a fit irrelevant;

3. a hit has to be part of a plane with a maximum of 2 hits. A hit recorded in a vertical event can have a very big Δy even though it's very close from the track. As this is the measure we will use to determine a mismatch, it is crucial to avoid this type of situation.

For each criteria, an example of a track that doesn't match it was plotted in fig. 6.9. This type of events or hits will be rejected from the analysis.

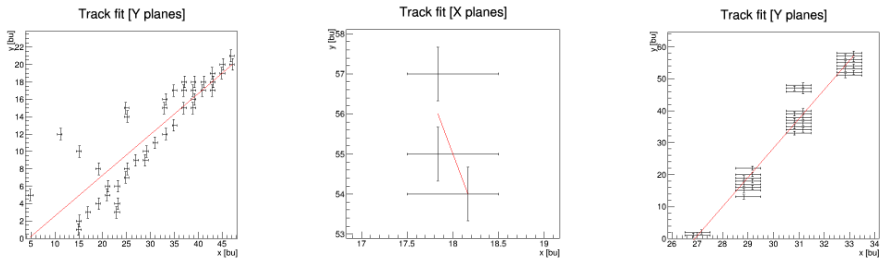

(a) (b) (c)

Figure 6.9: Event displays of tracks and hits excluded from the analysis: (a) the event is too messy (e.g. atmospheric shower), the fit is irrelevant; (b) not enough planes are hit to really constitute an appropriate track; (c) too many bars are hit within the same plane (vertical track) to appreciate the mismatch.

6.6 Processing

After eliminating all the unwanted hits, we are only left with perfectly suited signals to identify mismatched channels. The procedure consists in using Δy (described in the track reconstruction section) as our primary variable. It represents the distance between the COM of a bar and the reconstructed track, that is, for a given COM of coordinates (x_m, y_m), $\Delta y = y_m - (ax_m + b)$.

The critical secondary variables that we want to obtain for each channel are the ratios of mismatch. For each given integer distance i *bu*, we can calculate a ratio R_i that corresponds to the probability that a hit is within acceptable

range of a distance i *bu* off track. If we consider the distance distribution for a given bar $f(\Delta y)$, that ratio is defined as

$$R_i = \frac{\int_{i-2/3}^{i+2/3} f(\Delta y)\mathrm{d}(\Delta y)}{\int_0^{2/3} f(\Delta y)\mathrm{d}(\Delta y) + \int_{i-2/3}^{i+2/3} f(\Delta y)\mathrm{d}(\Delta y)}. \tag{6.3}$$

In the results section, only two of these ratios are presented because they suffice to prove our point. The first one for $i = 1$; although the first bin away from the track overlaps with the bin on track, it was chosen to change the lower boundary of the first bin to $(1 - 1/3)$ *bu* to cancel out the overlap and simplify the computation of the ratio estimation. The ratio subsequently reads

$$R_1 = \frac{\int_{2/3}^{5/3} f(\Delta y)\mathrm{d}(\Delta y)}{\int_0^{5/3} f(\Delta y)\mathrm{d}(\Delta y)}\,. \tag{6.4}$$

The other ratio is simply the rest of the distribution, that is

$$R_{\geq 2} = \frac{\int_{4/3}^{+\infty} f(\Delta y)\mathrm{d}(\Delta y)}{\int_0^{2/3} f(\Delta y)\mathrm{d}(\Delta y) + \int_{4/3}^{+\infty} f(\Delta y)\mathrm{d}(\Delta y)}\,. \tag{6.5}$$

If a bar is mismatched by more than one bar, it will appear clearly in that ratio, as all the hits will be located around a given distance i from the track and the ratio should be close to 1. Given an average distance $\overline{\Delta y}$, to simplify the computation, we degenerate the distribution of hits to a Dirac delta and we get

$$R_{\geq 2} = \frac{\int_{4/3}^{+\infty} \delta(\Delta y - \overline{\Delta y})\mathrm{d}(\Delta y)}{\int_0^{2/3} \delta(\Delta y - \overline{\Delta y})\mathrm{d}(\Delta y) + \int_{4/3}^{+\infty} \delta(\Delta y - \overline{\Delta y})\mathrm{d}(\Delta y)} = 1,\ \forall \overline{\Delta y} > 4/3\,. \tag{6.6}$$

It is trivial that this computation holds for broader distributions, as long as it doesn't overlap much more than 1 *bu* away from its centre point.

6.7 Mismatch ratio estimation

The use of triangular bars gives yet another challenge when it comes down to the identification of a mismatch. This geometry bounds a track to hit exactly two bars (or more but the post-selection process excludes the planes with more than 2 hits from the analysis). Considering the error bars chosen in a previous subsection and represented in fig. 6.6, a track could go through both bars and not be within 2/3 unit of the COM (black dot). An estimation of the expected rate in normal and mismatched channels is useful to be able to distinguish them.

Determining the probability of a mismatch in the EMR is divided in three steps. First, an angular distribution of the area accessible by a particle in a pair of bars $f_A(\theta)$ is calculated from geometrical arguments for an angle θ (a bigger area is equivalent to more events). Then, a mismatch Probability Density Function (PDF) $f_M(\theta)$ is obtained in the same fashion. Finally, a weighted average is calculated, using $w(\theta) = f_A(\theta) \times f_C(\theta)$ as the weight function, with $f_C(\theta)$ the cosmic muons angular distribution and θ the zenith angle. In all of these calculations, we use the units described in the previous subsection, the total area covered by the section of 2 bar is 2 bu^2.

6.7.1 Normal channels

In fig. 6.10, the figures represent 5 categories of angles that will result in different regimes and distributions to describe them. Each case will be considered separately and the functions assembled piecewise.

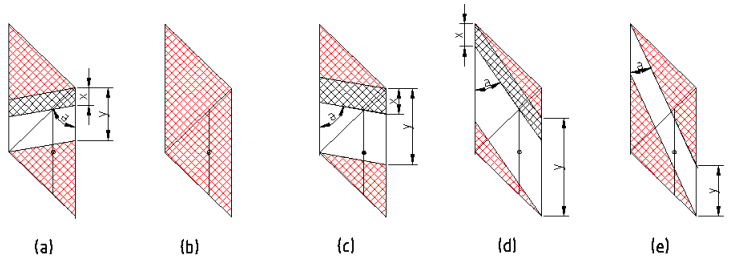

Figure 6.10: Area accessible and area mismatched in a pair of bars for different angles. Red areas don't produce hits in both bars and black areas are mismatched. The black dot is the centre of mass of the bottom bar.

a) $\boxed{-\pi/2 < \theta < -\pi/4}$

$f_A(\theta) = y = 1 - \tan(\pi/2 - \theta)$

$f_M(\theta) = x/y = \frac{\frac{1}{3}(1-\tan(\pi/2-\theta))}{1-\tan(\pi/2-\theta)} = \frac{1}{3}$

b) $\boxed{-\pi/4 < \theta < \text{Atan}(1/3)}$

$f_A(\theta) = 0$

$f_M(\theta) = 0$

c) $\boxed{\pi/4 < \theta < \pi/2}$

$f_A(\theta) = y = 1 + \tan(\pi/2 - \theta)$

$f_M(\theta) = x/y = \frac{\frac{1}{3}(1+\tan(\pi/2-\theta))}{1+\tan(\pi/2-\theta)} = \frac{1}{3}$

d) $\boxed{\text{Atan}(1/2) < \theta < \pi/4}$

$f_A(\theta) = y = 2 - (\tan(\pi/2 - \theta) - 1) = 3 - \tan(\pi/2 - \theta)$

$f_M(\theta) = x/y = \frac{\frac{4}{3} - \frac{2}{3}\tan(\pi/2-\theta))}{3-\tan(\pi/2-\theta)} = \frac{2}{3}\frac{2-\tan(\pi/2-\theta)}{3-\tan(\pi/2-\theta)}$

e) $\boxed{\text{Atan}(1/3) < \theta < \text{Atan}(1/2)}$

$f_A(\theta) = y = 2 - (\tan(\pi/2 - \theta) - 1) = 3 - \tan(\pi/2 - \theta)$

$f_M(\theta) = 0$

The area angular distribution has been normalized to a maximum area of 1 (which corresponds to 2 bu^2) and is plotted along with the mismatch PDF in fig. 6.11. They are the same for any couple of bars in the EMR. The last step is to combine f_A with f_C in order to get the weight and calculate the average. The cosmic muon distribution is not the same for the X and Y planes. They are both vertical but the bars are horizontal in the X planes and vertical in the rest. This means that the angular distribution of the muons must be shifted by $\pi/2$ radians. As a result, $f_{CX}(\theta) \propto \cos^2(\theta)$ [27] in X and $f_{CY}(\theta) \propto \sin^2(\theta)$ in Y. The weight functions $w_X(\theta)$ and $w_Y(\theta)$ (resp. for X and Y planes) are plotted in fig. 6.12. They are quite significantly affected by the orientation of the bars and are pretty much antagonist.

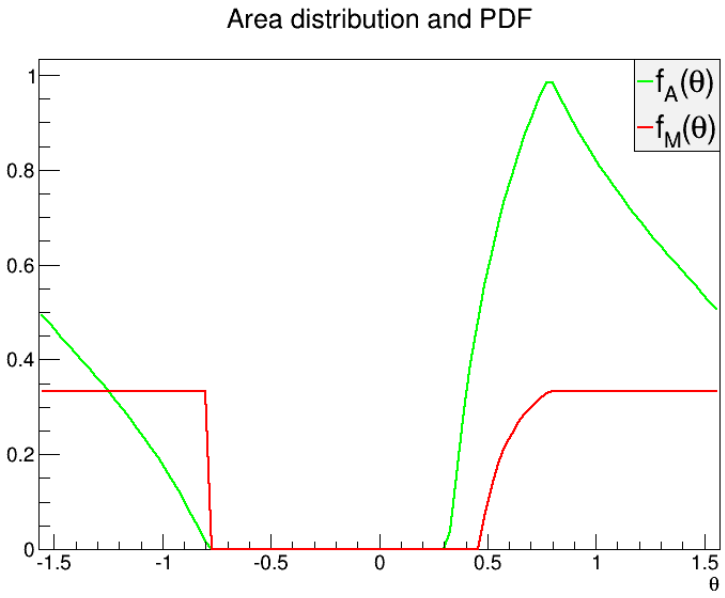

Figure 6.11: Area distribution and mismatch PDF of a cosmic muon going through the EMR at an angle θ with the zenith. At low angles (regime (b) in 6.10) there is always more than two hits and both functions plummet. At an angle of $\pi/4$, the entire area is accessible. Most of the time, the PDG corresponds to 1/3 of the area available.

The final step consists in calculating the weighted average of the mismatch probabilities p_{mX} and p_{mY} and they read

$$p_{mX} = \frac{\int_{-\pi/2}^{\pi/2} f_M(\theta) \times w_X(\theta) \mathrm{d}\theta}{\int_{-\pi/2}^{\pi/2} w_X(\theta) \mathrm{d}\theta} \simeq 25.3\% \tag{6.7}$$

$$p_{mY} = \frac{\int_{-\pi/2}^{\pi/2} f_M(\theta) \times w_Y(\theta) \mathrm{d}\theta}{\int_{-\pi/2}^{\pi/2} w_Y(\theta) \mathrm{d}\theta} \simeq 32.2\% \tag{6.8}$$

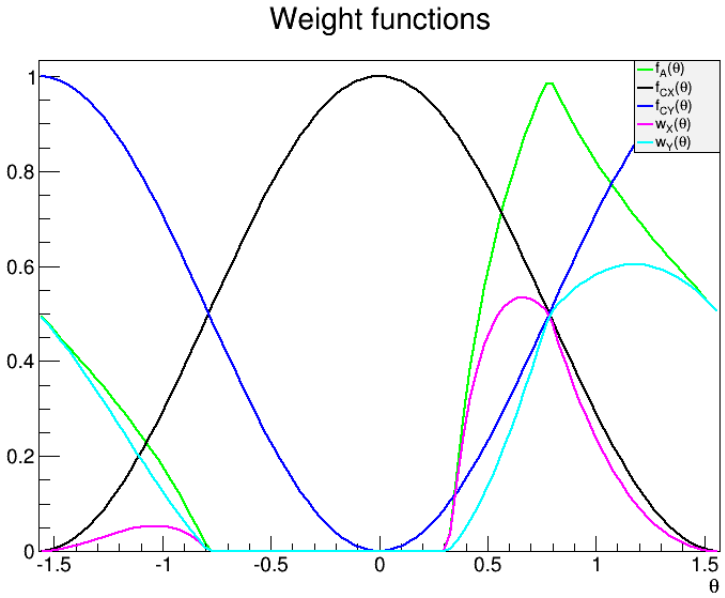

Figure 6.12: Weight functions of the mismatch ratios. Due to the shift between the two plane orientations, the weight function of each of them are opposite to each, one raises when the other plummets, which should give us different estimation of the predicted mismatch ratio.

6.7.2 Mismatched channel

As it appears in the causes section, a mismatch channel can never come alone. If one channel consistently produces hits one bin away from the track, we should have a similar mismatch in an adjacent bar. If we have a bar consistently 2 bins away from track, we should have the same mismatch two bars away, and so on. If there are any mismatched channels, they should come by pair.

The case in which two adjacent bars are swapped has to be treated separately from the other types. A particle going through one of the EMR plane produces hits in two adjacent bars (after post-selection, any other case is excluded). For a pair of mismatched channels, we have to consider two different cases. The particle can go through both of them or through one of them and a third channel. In the first case, the mismatch PDF obtained in the normal channel computation will stay unchanged. In the second, it will be impossible to have a hit in one of the bar, upping its mismatch PDF to 100%. As these two cases are equiprobable, we average them and get the estimated probability for mismatched adjacent bars p_{MX1} and p_{MY1} that read

$$p_{mX_1} = 62.6\%,\ p_{mY_1} = 66.1\%. \tag{6.9}$$

As for all the other distances, as the bars are not next to each other, all the PDFs are upped to 100% and we should observe something very close to that value in the eventuality of such mismatches,

$$p_{mX_i} = p_{mY_i} = 100\%,\ \forall i \geq 2. \tag{6.10}$$

6.8 Results

6.8.1 Adjacent bars mismatch ratio R_1

The ratio measured in each bar is plotted in a two dimensional histogram in fig. 6.13. By its side is a a plot of the distribution of ratio values. We can immediately notice that all the channels but two bunch into a Gaussian distribution on the left side of the plot.

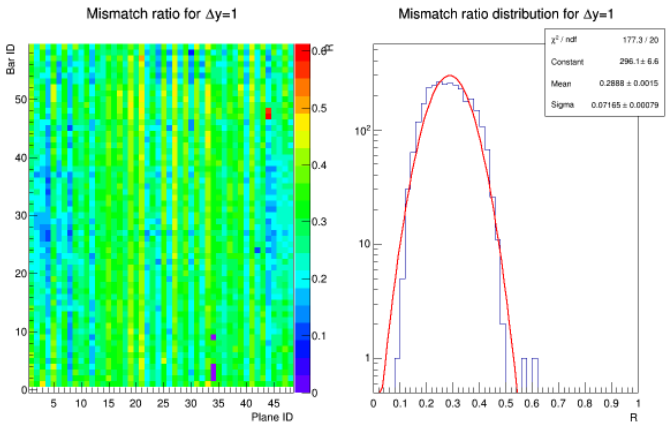

Figure 6.13: Mismatch ratio for adjacent bars. Most Two bars clearly stand out in the distribution and appear to be strong candidates for a mismatch.

Moreover, it is centred in 29.6%, which happens to be staggeringly close to what we estimated in the previous subsection. In fact, we found two values for the ratio depending on the orientation of the planes and, if these values are averaged, we get 28.7%. The width of the distribution can be explained by the fact that not every particle going through a bar actually ends up producing a hit. As a result, a particle could go through more than two bars but only leave two hits, complicating the geometry of the estimation. In addition, crosstalk has part to play in it as well as it produces hit where there shouldn't be any. Nevertheless, despite all the width of the distribution, two channels clearly stand out.

Plane ID	Bar ID	R_1
44	47	62.5±3.5%
44	48	57.2±3.2%

Table 6.1: Mismatch channel IDs and corresponding mismatch ratios

This anomaly is significant for several reasons. The first and most obvious reason is that they are next to each other. The probability of such an occurrence that wouldn't be caused by a mismatch is that much lower knowing that they are adjacent. Second of all, the uncertainty on these measurements is low enough that we can guarantee at 4 σ that they are not a statistical variation. The uncertainty for each bar and its distribution is compiled in fig. 6.14. Finally, the levels of ratio correspond perfectly with what we would expect from the es-

timation. The values found for their corresponding channel IDs are summarized in the tab. 6.1.

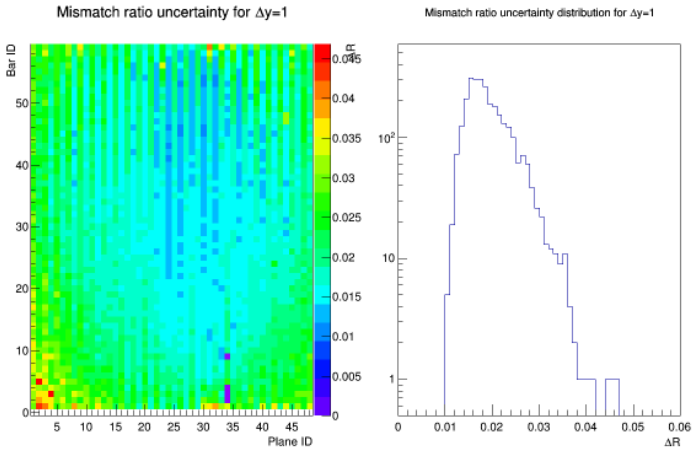

Figure 6.14: Mismatch ratio uncertainty for adjacent bars. Some bars at the corners of the detector have higher uncertainties because they recorded a lower amount of hits but are definitely not mismatched.

6.8.2 Other mismatches ratio $R_{\geq 2}$

The same analysis has been conducted for any other possible ratio and compiled in one plot in fig. 6.15.

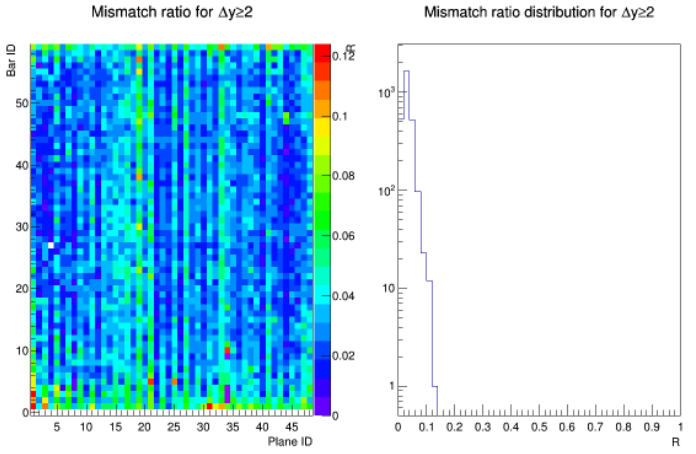

Figure 6.15: Mismatch ratio for bars further than adjacent. No significant deviation and nothing close to the predicted 100 %.

It clearly appears that the levels of mismatch are very low and are certainly not anywhere close to the 100% we would expect for this type of mismatch. As a result, no mismatch was be recorded for bars that are further that adjacent.

7 Crosstalk analysis

7.1 Causes

For each plane, crosstalk in the EMR happens in one critical location: the MAPMT. This is the place where all the fibres coming from the 59 bars come together in one place and the signals can get mixed up.

The first type of crosstalk we can encounter at this stage is optical crosstalk (OXT). A single fibre of the bundle can shine on more than one channel of the MAPMT mask. This phenomenon is depicted in fig. 7.1. The clear fibres are multi cladding fibres, 1.5 mm in diameter with 0.72 of numerical aperture [57]. The thickness of the layer of glass on top of the MAPMT channels can reach 0.8 mm [60]. This geometry allows a part of the light in the core of the fibre to leak onto other surrounding channels, even in the eventuality of fibres perfectly in contact and aligned with the photocathode. In the assumption that the bundle is perfectly against the mask and the light uniformly distributed in the fibre, we can compute the ratio of light leaked R_L to be

$$R_L = \frac{A_e}{A_c} = \frac{4(\pi R^2(\pi/2 - a)/\pi - R\sin(\pi/2 - a))}{\pi R^2} \simeq 6\% \tag{7.1}$$

with $R = 1.09$ mm the radius of the circle of light.

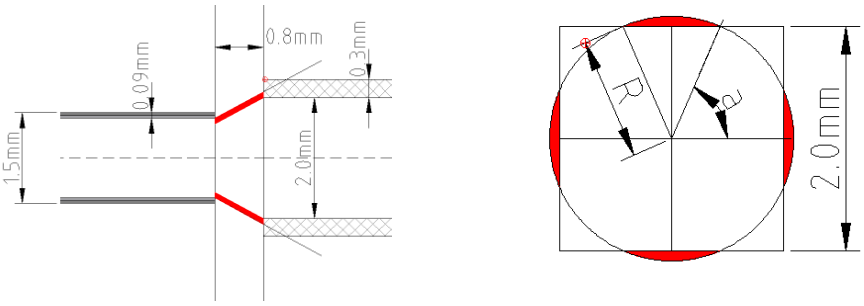

(a) (b)

Figure 7.1: Illustration of OXT in an MAPMT: (a) side view of a clear multi cladding fibre shining on one channel of the MAPMT; (b) Circle of light coming from the clear fibre and shining on the MAPMT channel. Both schematics clearly show how light can leak in the wrong MAPMT channel.

This standard level of light leak can vary for different reasons. On the one hand, the whole PMT mask can be shifted with respect to the centre of the fibre bundle (fig 7.2 (a)). In that case, the level of crosstalk measured in the surrounding channels of a given fibre will vary and this information will be used to determine the misalignment. On the other hand, a fibre is not always glued perfectly in the centre of its slot in the bundle. This effect can be seen on the picture of the bundle in fig. 7.2 (b) where the fibres aren't always exactly in the middle of the grid compartment. It will not affect the general crosstalk levels but can shift slightly the values from one fibre to another.

The other is anode crosstalk (AXT). A photo-electron can leak from a dynode to an adjacent accelerating structure and generate a signal in another channel

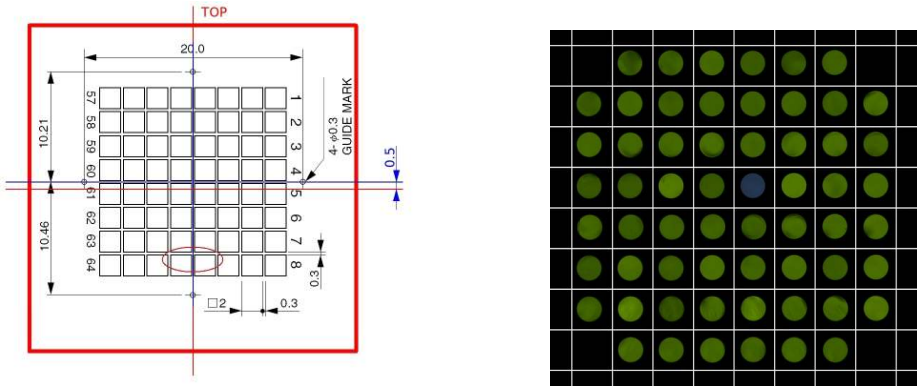

(a) (b)

Figure 7.2: Causes for crosstalk asymmetry: (a) technical drawing of the MAPMT mask, the red line represents a shift of the fibre bundle of 0.5 mm with respect to the mask; (b) clear fibre bundle, the fibres are not all glued in the same position in their grid compartment.

as represented in fig. 7.3. This a pretty well known phenomenon, the levels have been measured in house by Hamamatsu and are know to revolve around 1% of the initial signal in the adjacent channels for a 1 mm clear fibre lit by an incandescent light. This value depends mostly on the luminosity of the light and on the surrounding magnetic field [63]. In our set up, no magnetic field but the Earth's was present and it won't affect the analysis. This crosstalk will constitute a background for our measurements and won't be sensitive to a misalignment of the fibres.

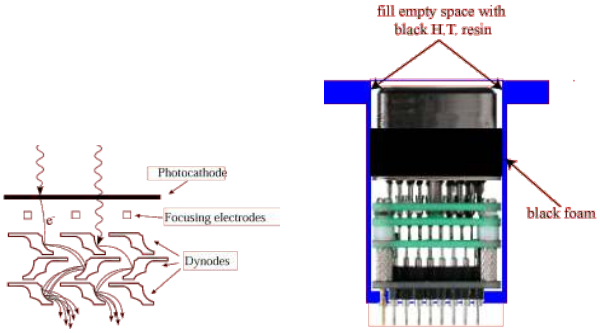

0.3	1.4	0.4
0.8	100	1.2
0.2	1.1	0.3

(a) (b) (c)

Figure 7.3: Illustration of AXT in an MAPMT: (a) schematic drawing of electrons leaking from one accelerating chain to another; (b) side cut of an MAPMT; (c) AXT levels measured in house in the H7546A Hamamatsu MAPMT [60].

7.2 Data acquisition

To measure the level of crosstalk, cosmic or beam data is not appropriate. As explained in the previous analysis, a particle always hits at least two bars within

the same plane and that renders an accurate crosstalk measurement impossible for two reasons. As we can see on the MAPMT numbered mask shown in fig. 7.4 (a), the light coming from two adjacent bars often ($\sim$ 86 % of the time) shines on two neighbouring channels of the MAPMT. In consequence, on the one hand, the primary signal energy resolution is quite gross as it's impossible to know if the whole signal comes from the energy deposited in the scintillating bar or if part of it emanates from crosstalk of the adjacent bar. On the other hand, a signal recorded in a neighbouring channel can't be attributed with certitude to crosstalk, as it could very well be a real signal.

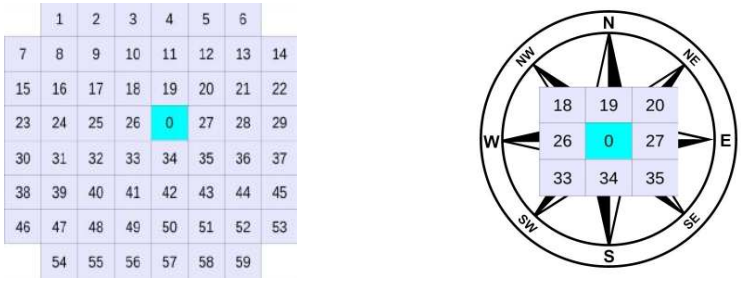

(a) (b)

Figure 7.4: (a) 60 channels MAPMT mask used in the EMR; adjacent bars in the detector produce light in adjacent channels. (b) Representation of channel 0 and the its surrounding; cardinal points are associated to each one of them.

For these reasons, an LED light source has been used to perform this analysis. As shown in 7.5 (a), an LED driver pulses light on diffusers that direct the light into a 48 fibres bundle. Each clear fibre conducts the light towards one specific channel of the MAPMT in all of the planes. It is labelled 0 and is surrounded by channels 18, 19, 20, 26, 27, 33, 34 and 35. For later purposes, these channels will be more intuitively renamed by cardinal points as represented in fig. 7.4 (b). The obvious advantage of this technique is that any hits in the aforementioned bars can only originate from crosstalk. The light coming from the LED driver is blue in contrast with the green light in other channels coming from the WLS fibres glued inside of the scintillating bars (fig. 7.5 (b)).

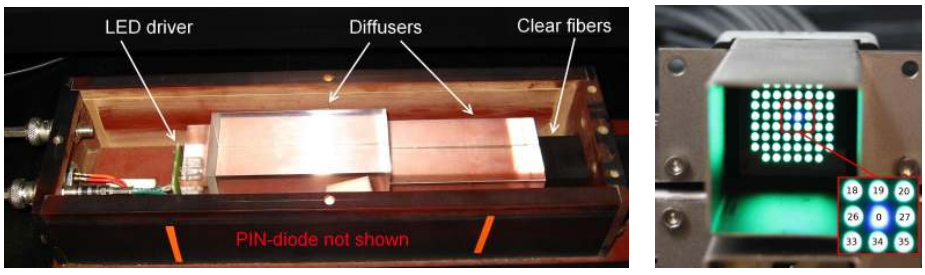

(a) (b)

Figure 7.5: Pictures of (a) the LED driver and (b) the fibre bundle output light.

When the data sample used in this master thesis was recorded, the EMR was fully operational and was located in the MICE hall at RAL. The LED driver

was tuned with a variety of voltages ranging from 11.0 V to 22.0 V by steps of 0.5V. The trigger was simple and consisted in the coincidence of an arbitrary spill gate and hits in a channel 0. For each one of them, 100 spills of 100 triggers were recorded to reach a total of 10000 triggers per setting.

7.3 Events structure

Each hit in channel 0 can generate hits in the surrounding channels. The 4 channels directly adjacent to it (N,S,W,E) are obviously the most likely to receive a signal. The 4 corners surrounding the test channel (NW,NE,SW,SE) are less likely to be shined on but will be included in this analysis. The channels located two or more compartment away from the channel 0 are so unlikely to register a hit that they are not taken into consideration. In fig. 7.6, we can see the amount of hits, the integrated Time of Threshold and the total charge for two different data samples.

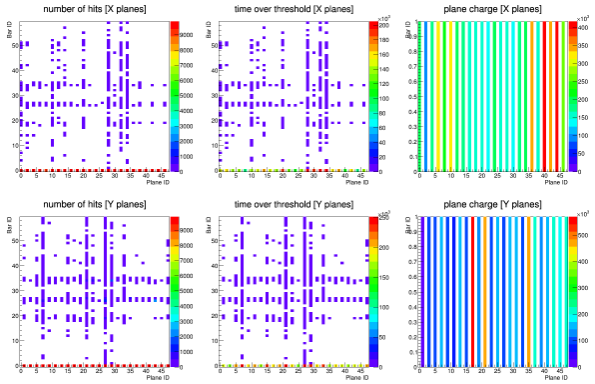

(a)

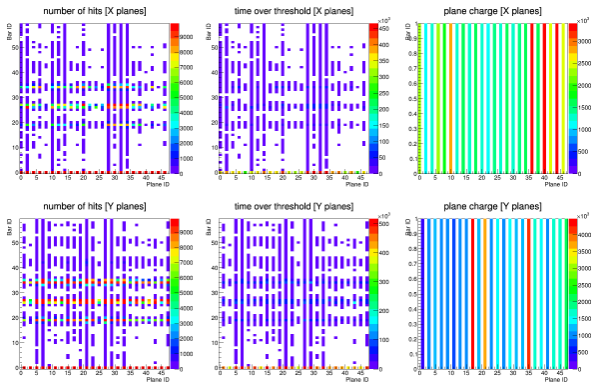

(b)

Figure 7.6: Integrated amount hits, Time over Threshold and charge over 10000 LED triggers at different settings: (a) one corresponding to MIP energy deposition and (b) the other to a particle stopping in the detector or an energetic shower.

On the one hand, in both cases, we clearly see four lines appearing at the level

of bars 19, 26, 27 and 34 as we would expect. There is a noticeable unbalance from one plane to another. While some plane barely experience crosstalk, some planes record hits in every single bar at least once during a run. Moreover, their corresponding integrated charges and Time over Threshold aren't even. This comes from the MAPMTs irregularities and lack of calibration at the time of this analysis. Nevertheless, it won't affect our results as the planes are analysed one by one and that the energy measurement is always consistent with other measurements taken within the same plane. On the other hand, it appears very clearly that the amount of hits, although constant in channel 0, is clearly much higher in the adjacent channels at high voltage. Some surrounding bars are hit practically every single time a signal in channel 0 is recorded.

One final interesting element is the energy and time distribution. To represent it clearly, a high voltage LED setting was chosen and is given in fig. 7.7. As we've seen before, the levels of crosstalk for high voltages are very high and hence create a clear bunch on the distribution. The very high energy hits (ToT$\sim$ 45) are the primary hits in channel 0. The lower energy hits (ToT$\sim$ 5) are secondary and correspond to crosstalk in adjacent bars. We can see that the crosstalk signals are easily discriminable as they are both lower in energy and shifted in time (typically 10 ns). The amount of hits is much higher at low energy because a given light pulse can only generate one signal in the test channel but can give rise to a wild array of hits in the surrounding ones.

The cuts applied on each data sample are rudimentary. The only requirement to associate a hit with a given LED setting is that its timing coincides with the trigger time. In terms of trigger time minus hit time Δt, it corresponds to the interval 25 ADC counts $< \Delta t <$ 40 ADC counts.

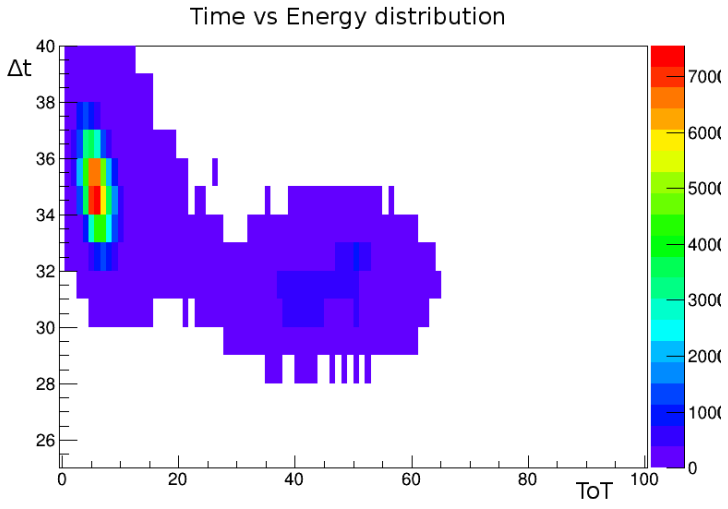

Figure 7.7: Energy and time distribution of a high voltage data sample. Two bunches appear on the distribution: one at very high energy (ToT$\sim$ 45) corresponding to the primary signals in channel zero and a much higher bunch at lower energy (ToT$\sim$ 5) associated with the crosstalk. Both axis unit is ADC counts.

7.4 Setting selection

For each setting and plane, we yield a Time over Threshold distribution in channel 0 as well as a charge distribution. Two of the raw data sample (18.5 V and 21.5 V) failed to unpack and were thus excluded from the analysis. If we plot the Time over Threshold (ToT) average and RMS as a function of the voltage in one plane, we get, for instance, fig. 7.8. We can easily grasp the logarithmic structure that we would expect from this type of measurement. A similar plot for the total charge gives a linear progression. The green area represents the voltage region for which the recorded Time over Threshold are consistent with values we would get for cosmic muons. High voltages match the energy deposition pattern of a muon stopping in the EMR or a very energetic electromagnetic shower.

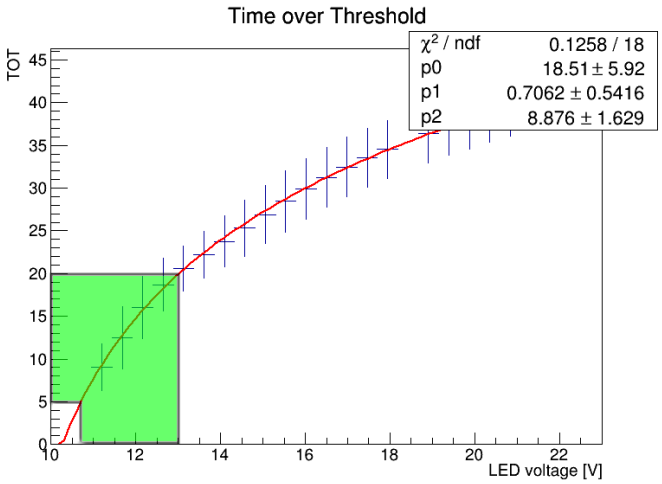

Figure 7.8: Time over Threshold distribution as a function of the voltage applied to the LED driver. The green area corresponds to Time over Threshold distribution similar to an MIP one.

The problem with LED runs is that they don't straight forwardly correspond to a given particle energy deposition. To tackle this problem, cosmic data was recorded at RAL in the same experimental condition. Then, a distribution of ToT measurements was plotted for each plane in the EMR and saved in a ROOT file. These histograms were then used as a tool to identify, for a given plane, the LED voltage that simulates a cosmic distribution the best. The method used was to loop over the first 10 settings, calculate the area $\mathcal{A}$ between the two normalized distributions and select the setting that gives the lowest value to be the MIP run. Mathematically this boils down to minimizing:

$$\mathcal{A}(V) = \int_0^{+\infty} \mid f_C(\mathrm{ToT}) - f_{LED}(\mathrm{ToT}, V) \mid \mathrm{dToT}, \tag{7.2}$$

with f_C the cosmic ToT distribution and f_{LED} the LED one. A comparison of the two type of distribution is provided in fig. 7.9. We can see that the LED distribution is sharper but will still give us a good estimation of the crosstalk associated with an MIP energy deposition pattern.

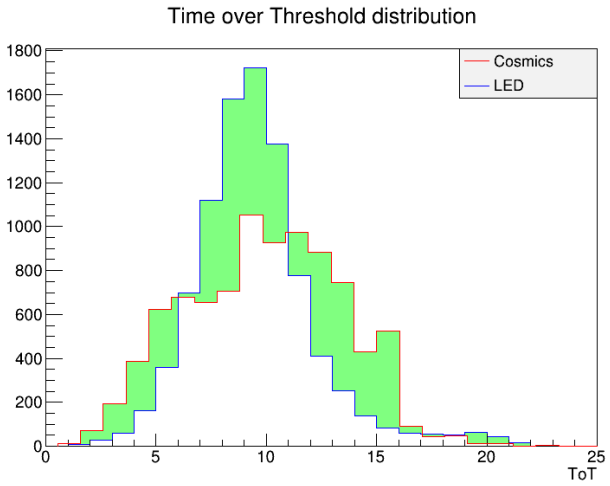

Figure 7.9: Normalized distributions of Time over Threshold measurements of both cosmic and LED data in plane 3. The green area has to be minimized to achieve the most accurate estimation of the crosstalk at MIP energies.

7.5 Processing

The crosstalk level can be characterized by two main measurements.

The first parameter is the **ratio** R_Q between the signal amplitude in a given adjacent channel over the primary amplitude in channel 0. It is indeed very important to know what is the percentage of light that leaks in a given surrounding channel to see if the measurement of a signal in the EMR is significantly altered by it. The challenge in making a sensible measurement of this value is twofold and related to the Time over Threshold (ToT) measurement. On the one hand, we expect to measure signals only above a certain value. Digitization simulations have shown that a single photo-electron generated at the beginning of an accelerating section in the MAPMT generates a signal with a ToT of a few ADC counts. As the resolution on this measurement is of 1 ADC count, the ratios involving low values of ToT in channel 0 will be dramatically biased by this phenomenon. A way of coping with it is to rely on the higher voltage settings to provide a value of the ratio R_Q. On the other hand, ToT measurement are not linearly proportional to the signal amplitude. As a result, if a ratio of ToT measurements was calculated, they would not correspond to an energy ratio. The exact dependency between ToT and the charge Q wasn't thoroughly investigated in the scope of this crosstalk analysis but we would expect an exponential behaviour of the form

$$Q = e^{a \times \mathrm{ToT} + b} \tag{7.3}$$

with a and b two unknown parameters. a is the slope of the exponential in log scale and depends on the EMR characteristics such as the scintillation time constant, the FEB shaping function or the threshold level. As a result, we expect it to be constant for each plane with small variations. The parameter b, on the other hand, depends on the two PMTs gain and can vary significantly from one plane to another. These parameters were obtained experimentally by

fitting the charge Q vs ToT graph for each plane with an exponential law; the fitting worked remarkably well and an example is given in fig. 7.10. Underneath are plotted the distributions of these parameters throughout the planes.

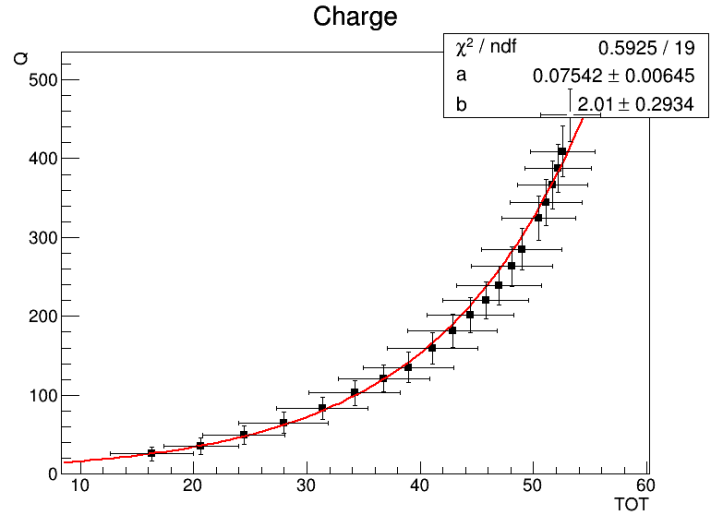

(a)

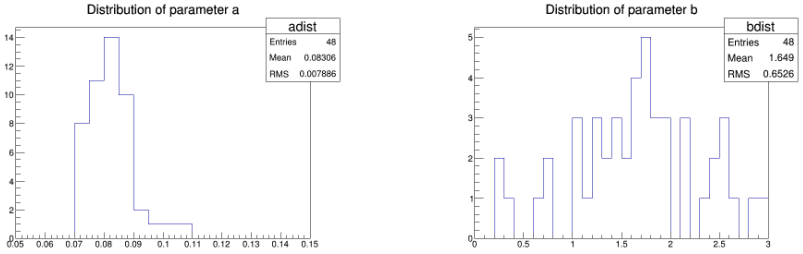

(b) (c)

Figure 7.10: (a)Exponential fit of the Q vs ToT graph of plane 40 with an exponential of the form $Q = e^{a \times \mathrm{ToT} + b}$. (b),(c) Distributions of the exponential parameters a and b over all the planes. The parameter a stays close to constant throughout the planes while b varies significantly .

These fitted parameters are then used to convert the ToT measurements into charge measurements to calculate the ratio R_Q. If we measure a ToT ToT_i in one of the neighbouring channel and ToT_0 in the test channel, then the ratio reads

$$R_Q = \frac{Q_i}{Q_0} = \frac{e^{a \times ToT_i + b}}{e^{a \times ToT_0 + b}} = e^{a(ToT_i - ToT_0)} \,. \tag{7.4}$$

The second main parameter used to characterize the crosstalk is the **rate** at which crosstalk happens needs to be evaluated. The actual quantity that we measure is the ratio R_N of hits in a given surrounding channel N_i to the total amount of hits in channel 0 N_0, i.e. $R_N = N_i/N_0$. This quantity is measured in each of the 8 surrounding channels for the MIP run.

7.6 Results

7.6.1 Individual plots

This analysis produced a plethora of graphs for each plane that obviously can't all be included in the core of this paper. Most of them are compiled plane per plane in [64] and a few of them are presented in this section to explain their significance. For each plane, we gather the following graphs:

I. Q vs ToT;

II. ToT vs Voltage;

III. Q vs Voltage;

IV. for each of the 8 channels around 0:

   (a) ToT_i vs ToT_0;

   (b) R_Q vs Q_0;

   (c) R_N vs ToT_0.

The eight plots for of the first series (IV.(a)) are given for one plane in fig. 7.11. The values given for ToT_i are averaged over one voltage setting.

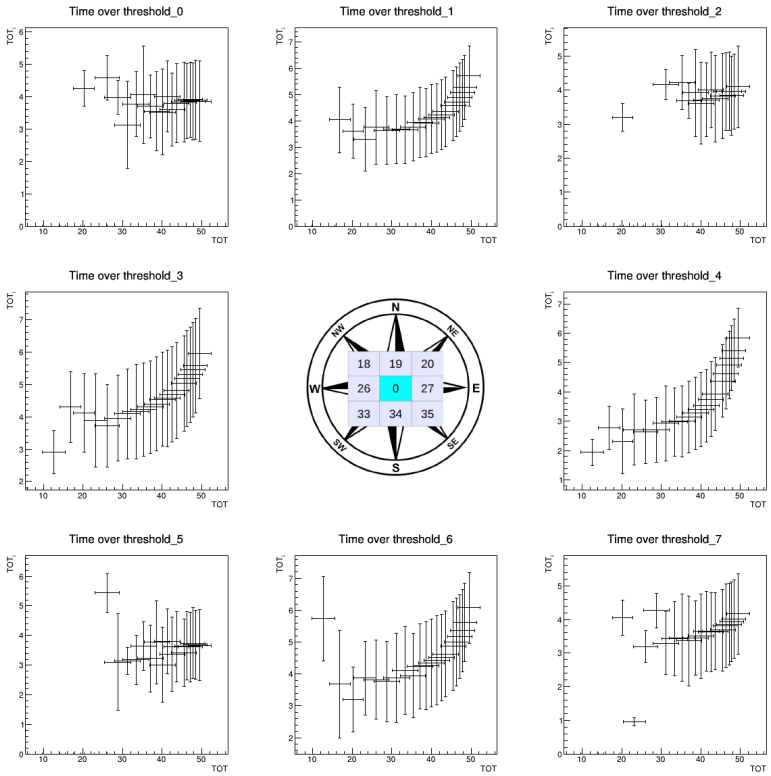

Figure 7.11: ToT_i in the surrounding channels as a function of the primary signal. It stays constant at low ToT_0 and raises after a certain threshold.

It appears clearly in the four channels directly adjacent to channel 0 (N,S,W,E) that, after a small flat stretch, the Time over Threshold starts raising exponentially as a function of the signal intensity. This is the behaviour we would expect from the digitization simulations; the minimum we observe revolves around 4 ADC counts. Nevertheless, in the 4 corners, we don't see a clear detachment of the curve from the threshold level. This makes sense as the light leaked in the corners is not as bright as in the adjacent channels and is hence unlikely to tear off more than one photoelectron.

The second series of plots (IV.(b)) corresponding to the ratio R_Q are represented for a given plane in fig. 7.12. The values correspond to averages and each of the points to an LED setting.

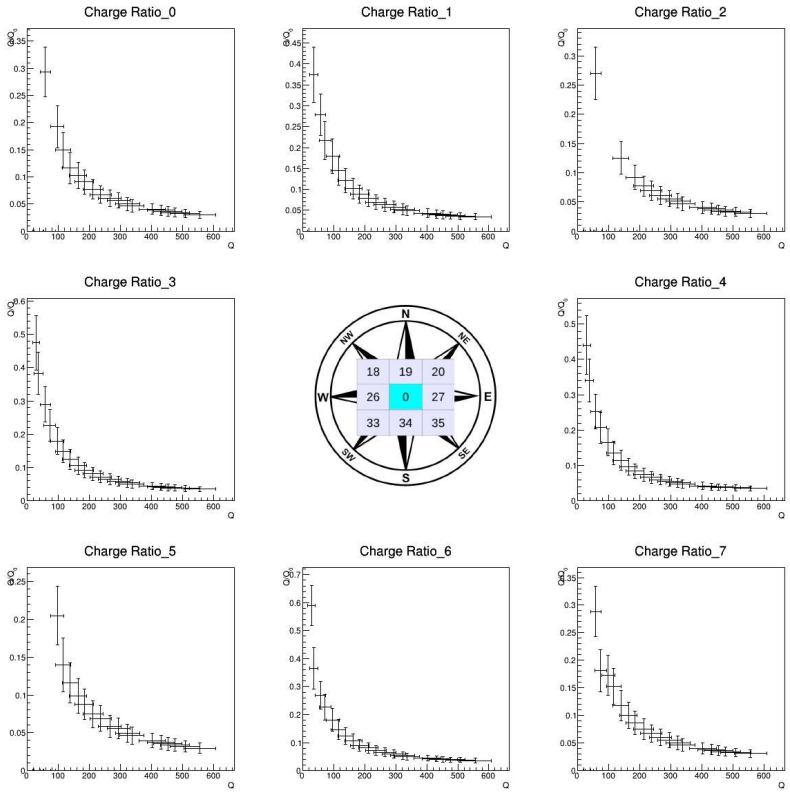

Figure 7.12: Crosstalk signal ratio R_Q as a function of the charge in channel 0. The ratio decreases as $\sim 1/Q$ before stabilizing in the adjacent channels.

This should be constant as a function of Q_0 because the crosstalk signals charge Q_i are linearly dependant on the primary signal charge. The reason why it isn't is because of the threshold behaviour of the ToT measurements. In these plots we have two different regimes. Before the ToT_i passes the threshold, it is a constant and, as a result, so is Q_i and we get $Q_i(Q) \sim 1/Q_0$. After the threshold is overcome, the function stabilizes and reaches a constant, as we would expect. We don't see that stabilization in the corners as they never reach that threshold. For each channel, the value of R_Q measured for the highest energy setting is chosen to be the reference crosstalk value. In the corners, as the threshold is

never reached, the values only represent an upper boundary.

Finally, the third series of plots (IV.(c)) corresponding to the crosstalk rate R_N for a given plane are plotted in fig. 7.13. The 8 graphs on the sides of the picture correspond to the eight surrounding channels as for the previous sets of plots. The central graph represents the integrated rate of crosstalk, i.e. the probability that at least one of the surrounding channels received a signal when channel 0 did.

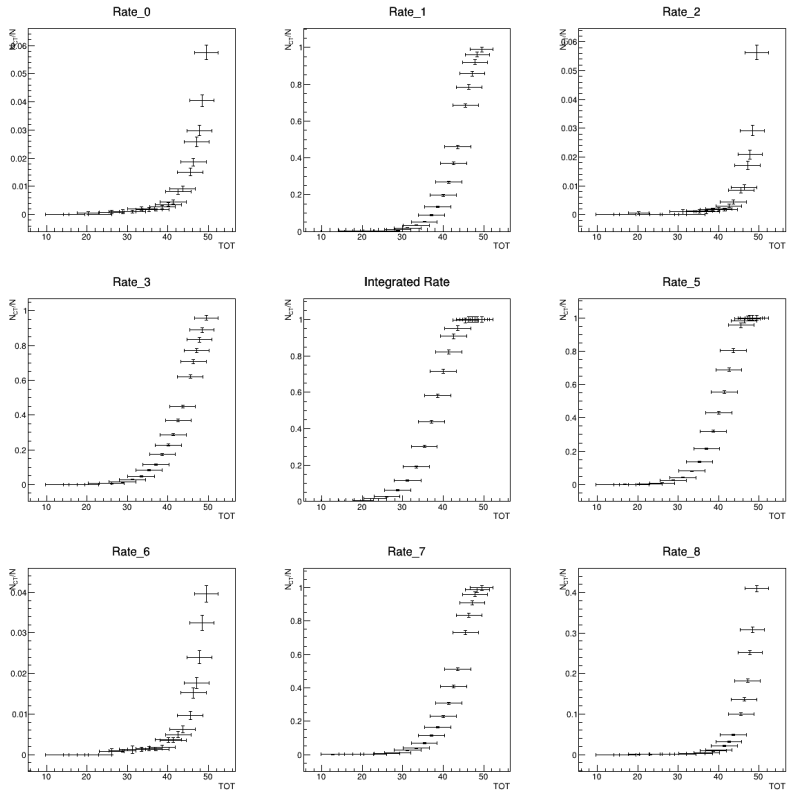

Figure 7.13: Crosstalk rate R_N as a function of the ToT in channel 0. Close to 0 % at low ToT_0, it raises close to 100 % for very high energy depositions.

It appears that the probability of crosstalk at low voltage (which corresponds to our MIP run) is very low. It increases as a function of the signal amplitude and sometimes reaches 100% at high voltages. This is the behaviour we expected.

7.6.2 Summary

The values found for the ratio R_Q and the rate R_N are compiled in tab. 7.1 for each separate plane. R_Q is the value of the ratio measured for the highest voltage setting and R_N the rate measurement in the MIP run.

The quantities for the corners are not displayed for two reasons. The ratio calculated for them would only give an upper limit and their rate almost always has an uncertainty as big as its value because of the low amount of hits recorded

in them. A way to get a better estimation would be to rerun this analysis with a much higher number of LED triggers.

Nevertheless, what we get here is reassuring. For all the planes, as depicted in fig.. 7.14 and 7.15, the probability of crosstalk is mostly under 0.5 % and, if crosstalk there is, the signal recorded in the adjacent channels only represents 4.5 ± 1.5 % of the initial signal

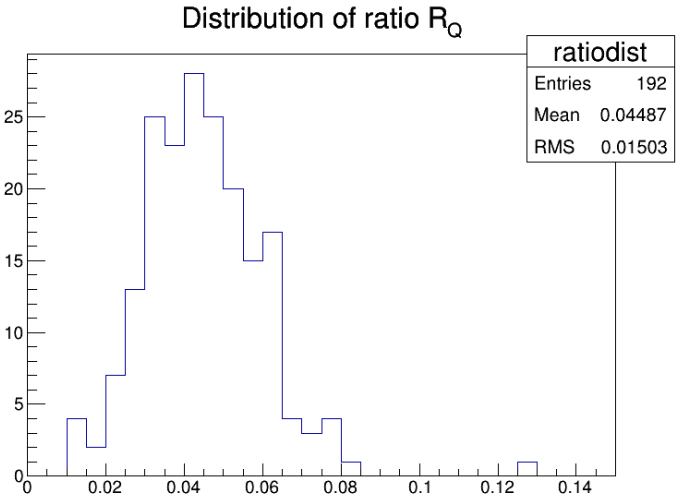

Figure 7.14: Crosstalk ratio R_Q distribution. The average signal intensity in adjacent channels is distributed around 4.5 % of the initial signal.

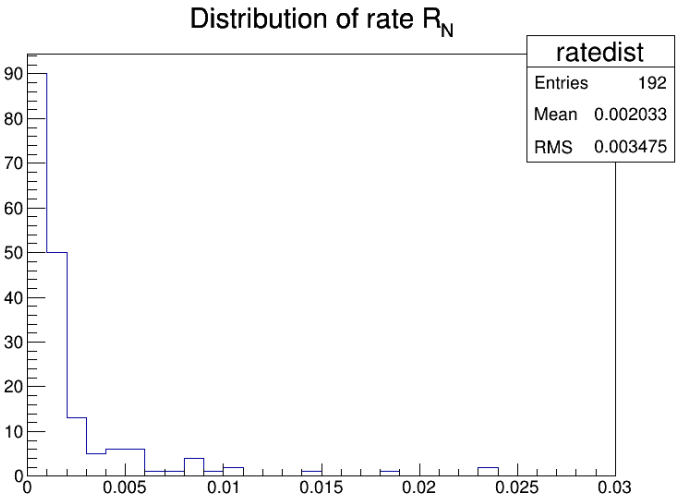

Figure 7.15: Crosstalk rate R_N distribution. Most of the channels adjacent to a primary signal experience crosstalk less than 0.5 % of the time.

Plane ID	Ratio R_Q [%]				Rate R_N [%]				
	N	W	E	S	N	W	E	S	Int.
1	4.0	4.3	4.3	4.6	0.4	0.1	0.3	0.2	0.6
2	3.7	3.8	4.9	4.1	0	0.1	0.5	0.1	0.6
3	4.0	6.0	3.4	3.6	0.1	0.1	0.1	0.2	0.3
4	5.5	5.7	5.3	6.3	0	0	0	0.1	0.1
5	4.6	4.6	4.6	5.1	0.1	0	0.1	0.1	0.1
6	3.3	4.1	3.3	3.3	0.1	0.5	0.1	0.1	0.7
7	5.8	6.1	5.8	7.9	0.1	0.1	0.1	0.1	0.1
8	3.2	3.8	3.2	3.3	0.3	0.2	0.4	0.7	1.5
9	5.5	6.1	5.1	5.8	0.1	0.1	0.1	0.1	0.1
10	4.7	4.8	4.4	5.0	0.1	0.2	0.1	0.1	0.3
11	5.9	7.6	5.8	6.1	0.2	0.8	0.1	0.2	1.2
12	2.6	2.5	2.8	2.6	0.1	0.1	0.1	0.1	0.1
13	6.5	6.8	6.3	7.2	0.1	0.1	0.1	0.2	0.5
14	3.2	3.2	3.3	4.3	0	0	0.1	0.1	0.1
15	4.1	4.5	4.3	4.2	0.1	0.1	0.3	0.1	0.4
16	1.1	1.2	1.1	1.4	0.1	0.2	0.2	0.5	1.1
17	3.9	4.2	4.0	4.4	0.1	0.1	0.1	0	0.1
18	3.5	3.5	3.5	3.6	0	0.1	0.1	0.1	0.1
19	4.3	4.7	4.1	5.2	0.1	0	0	0.1	0.1
20	3.2	3.4	3.0	3.4	0	0.1	0.1	0.1	0.1
21	4.2	4.7	4.4	5.1	0.1	0.2	0.2	0.2	0.6
22	2.5	2.7	2.7	2.3	0.3	0.6	0.8	1.5	3.9
23	5.7	6.3	5.7	6.6	0.1	0.1	0	0	0.1
24	2.1	2.6	2.8	3.4	0.2	0.3	0.5	0.3	1.3
25	6.6	8.3	6.5	7.6	0	0.1	0	0	0.1
26	4.2	4.7	4.1	3.9	0	0	0	0.1	0.1
27	5.1	5.5	4.8	5.2	0	0	0	0	0
28	2.2	2.4	1.9	2.0	0.9	2.4	0.6	1.0	5.6
29	3.2	3.5	3.3	3.6	0.2	0.2	0.2	0.2	0.8
30	3.2	3.6	3.1	4.8	0.1	0.3	0.2	3.1	3.9
31	4.4	3.8	4.3	4.4	0.1	0.1	0.1	0	0.1
32	4.9	4.6	5.5	4.9	0	0	0.2	0	0.2
33	3.3	3.9	3.7	3.6	0.1	0.3	0.2	0.2	0.4
34	2.4	2.3	2.4	2.1	0.1	0.2	0.2	0.3	0.4
35	4.5	4.7	4.4	4.6	0.1	0.2	0.2	0.1	0.6
36	3.7	3.6	5.7	3.8	0.2	0	0.4	0	0.4
37	4.3	4.4	4.3	4.4	0	0	0	0	0
38	3.9	3.7	3.6	3.4	0.1	0.1	0.1	0.1	0.1
39	3.8	3.7	3.6	3.6	0.2	0.1	0.1	0.1	0.2
40	3.2	3.1	3.3	3.4	0	0	0	0	0
41	6.1	6.4	7.1	6.0	0	0	0	0	0
42	6.4	7.3	6.4	7.5	0	0.1	0	0	0.1
43	4.8	5.0	4.6	5.5	0	0	0	0	0
44	5.1	12.6	5.1	5.1	0.1	2.4	0.1	0	2.4
45	5.9	6.1	6.2	6.2	0	0	0	0	0
46	5.2	5.2	6.5	5.7	0	0	0.1	0.1	0.1
47	5.3	6.2	5.1	5.6	0.1	0.1	0	0.1	0.1
48	2.3	2.6	2.5	2.7	0.1	0.1	0.1	0.2	0.3

Table 7.1: Ratio and rate of crosstalk in percent

8 Misalignment

8.1 Processing

The data sample used to measure the misalignment of the MAPMT is the same LED data that was processed in the previous section.

For each plane, the quantities we seek to evaluate are the coordinates of the MAPMT mask centre (x_C, y_C) with respect to the fibre bundle mask centre. To reconstruct the position of this point, we use the crosstalk phenomenon at our advantage. The idea is that, if a mask is shifted with respect to the fibre bundle, light will leak and create a signal more often in some channels than others. Subsequently, we calculate a weighted average of the form

$$(x_C, y_C) = \left(\frac{\sum_i x_i w_i}{\sum_i w_i}, \frac{\sum_i y_i w_i}{\sum_i w_i} \right) , \tag{8.1}$$

with x_i, y_i the coordinates of the surrounding channels and w_i the amount of hits recorded in them; the coordinate system used for this analysis is represented in fig. 8.1. We can infer an uncertainty on this measurement that will be directly be connected with the amount of hits in the surrounding bars, that is, for the first coordinate,

$$\Delta x_C = x_C \left(\frac{\bigoplus_i x_i \sqrt{w_i}}{\sum_i x_i w_i} \oplus \frac{\bigoplus_i \sqrt{w_i}}{\sum_i w_i} \right) . \tag{8.2}$$

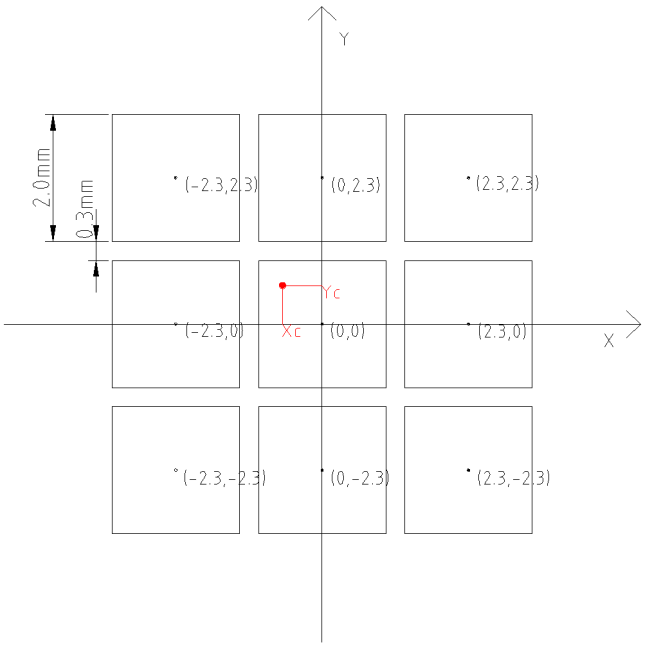

Figure 8.1: System of coordinates used to determine the misalignment centre. Channel 0 is defined as the origin of the axis while the surrounding channels are set according to their distance, in mm, from the centre of channel 0.

8.2 Results

8.2.1 Graphs

The definition of the misalignment centre and of its uncertainty gives us a clear idea of what setting should be chosen. It is trivial that higher primary signals in channel 0 are more likely to produce crosstalk than lower ones. For this reason, the higher the voltage, the larger the amount of hits in the surrounding channels and the smaller the uncertainty on the coordinates. This is illustrated in the graph of fig. 8.2. The points with broader uncertainties correspond to low voltage settings and we can notice a significant precision improvement at higher voltages. It is important to notice that the points cluster at the end of the trail and this phenomenon makes it relevant to choose the highest energy setting.

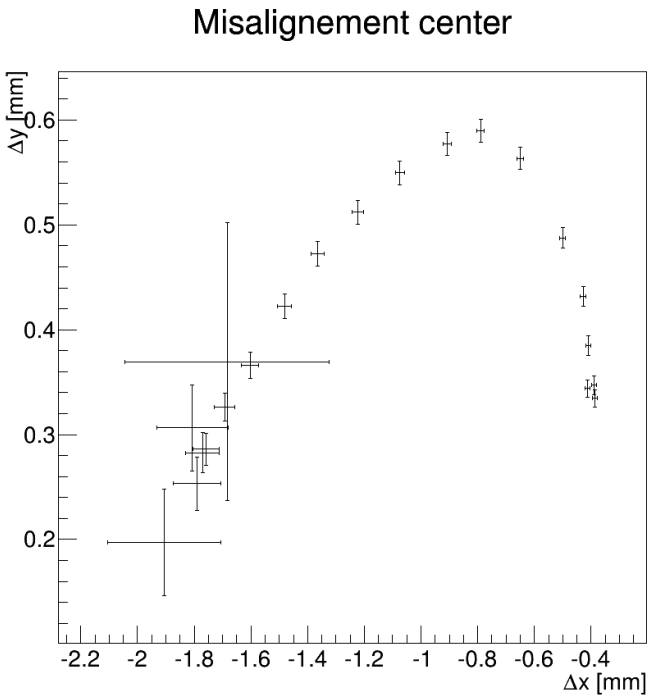

Figure 8.2: Misalignment centre of plane 2 for different LED settings. The points with broad uncertainties correspond to low crosstalk and, as it increases, the points become more accurately defined.

Another plot is shown in fig. 8.3 representing the misalignment centres for each plane to see if there is any particular tendency for the MAPMT mask to be shifted in one particular direction. The tags on each correspond to the plane ID. There is a noticeable cluster of planes around $(-0.3, 0.3)$, part of which can be explained by the fact that the mask is shifted, by design, of -0.5 mm along the x axis. These are not major shifts and, although they have consequences on the crosstalk geometry, they won't influence range reconstruction in the EMR.

An exhaustive list of the misalignment centres is provided for all the planes

in [64].

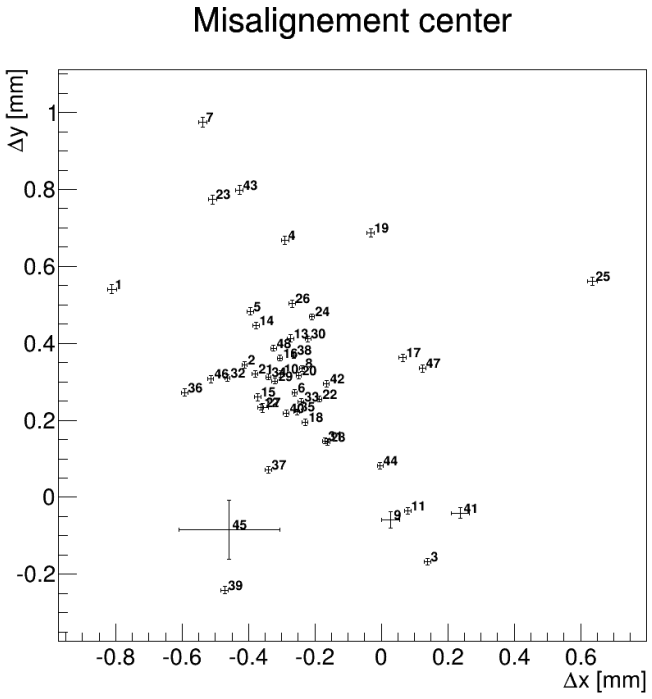

Figure 8.3: Distribution of the misalignment centres of the 48 planes. Most of them cluster around a value of $(-0.3, 0.3)$. The points with broader uncertainties correspond to planes that are less likely to experience crosstalk.

9 Signal acquisition efficiency

9.1 Definition

This analysis aims to determine the probability for a signal to be lost in the EMR. The critical requirement in this detector is to have at least one hit in each plane. If a plane is lost for an EMR module on the path of the particle, information on one of the coordinates is lost and range reconstruction accuracy is decreased. In this context, it is necessary to determine if signal loss is a predominant factor that should be asserted in the EMR. The signal acquisition efficiency E_{SA} is defined as the probability that an MIP muon will leave at least a hit in a plane that it crosses.

More specific quantities have been measured in the context of this analysis. First of all, the evolution of the efficiency as a function of the selected plane. This measured parameter depends on each MAPMT's characteristics and selected voltage. As a result, if one plane MAPMT does not respond as well as the others, the efficiency will be lower. Second of all, the dependency between the production of a signal and the energy deposited in a scintillating bar has been measured using digitized Monte Carlo simulation. Finally, the distribution of the amount of bars hit per plane was calculated.

9.2 Data acquisition

Several data samples were used for this analysis to assert the influence of energy deposition on the amount of bars hit in one plane.

Using muons that stop in the detector allows us to appreciate the influence of energy deposition on the amount of bars hit (i.e. crosstalk). Nevertheless, this won't allow us to analyse the most downstream planes behaviour. To tackle this issue, two additional settings with much higher energy were selected to probe every last plane of the detector. Monte Carlo studies of the EMR have shown that muons with momenta p_z above 280 MeV/c should leave the detector without stopping [65]. The four chosen settings fit as two of them being under that predicted value and two far above. The data samples processed in this analysis are summarized in tab. 9.1 and have been extracted from MICE Step I data recorded in October 2013.

Each setting used provides us with a value of the momentum at target from

Run ID	Setting	Trig.	p_z^{Q9} [MeV/c]	p_z^{EMR} [MeV/c]
5428	e^+	60511	300.38	239.64
5429	e^+	21860	300.38	239.64
5439	π^+	17265	293.83	232.87
5450	π^+	55823	293.83	232.87
5401	π^+	90757	424.37	365.29
5403	π^+	37969	424.37	365.29
5405	π^+	30007	424.37	365.29
5410	π^+	50670	450.17	388.77
5414	π^+	37969	450.17	388.77

Table 9.1: Beam settings momenta chosen for the signal efficiency analysis.

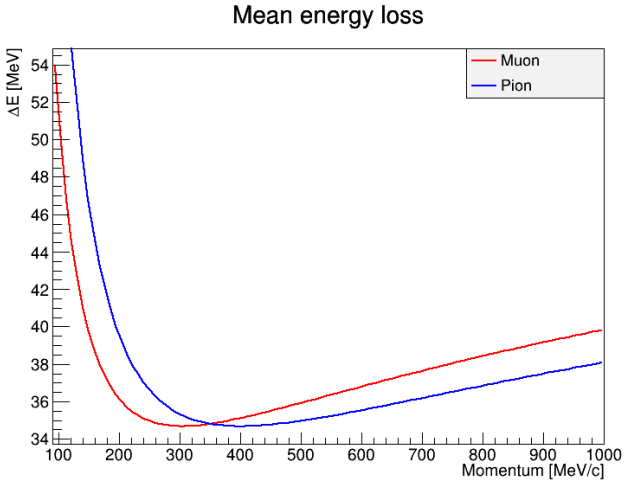

Figure 9.1: Bethe function of the energy lost in KL through multiple ionizations by muons (red) and pions (blue). The energy lost by an MIP muon is ~ 35 MeV.

which the momentum upon exiting Q9 (ninth quadrupole of the MICE set-up) has been computed using Monte Carlo simulations of the MICE beam line. After Q9, the beam still goes through two Time of Flight detectors (TOF1 and TOF2 [47]), 9.48 m of air (between the two TOFs) and an lead based calorimeter (KL [51]). The mean energy loss in the TOFs and the air has been previously evaluated and estimated to be 10.12 MeV in each TOF and 1.6 MeV in the air [66]. A simplified estimation of the mean energy loss in KL was developed specifically for this analysis and is plotted for muons and pions as a function of the energy in 9.1. These functions have been computed using the relativistic Bethe formula [42] corresponding to the KL composition. Applying these losses to the a given energy at Q9 provides us with a good estimation of the momentum upon entrance of the EMR.

For the Monte Carlo simulation, a simple 250 MeV/c negative muon was fired at the detector with a typical angular distribution. 10000 events were generated for this task.

9.3 Hit pre-selection

In this analysis, only the muons are used to calculate the efficiency. As a result, some kind of filter has to be used to discriminate the other particles and select the muon events. The tool that has been chosen to perform this task is the time of flight between TOF1 and TOF2 [47]. The MICE events that only produced one hit (i.e. a pair of slabs) in TOF1 and TOF2 are selected and the Time of Flight is computed. The distribution of times is plotted as shown in fig. 9.2 and we clearly see three peaks appearing. The three bumps are identified using ROOT TSprectrum class, fitted by a triple Gaussian and a probability of belonging to each peak is provided for every event. The leftmost Gaussian function corresponds to relativistic particles, i.e. electrons or positrons. The two others are the muon and the pion peak, clearly separated thanks to the difference of mass between the two particles ($m_\mu = 105.66$ MeV/c^2, $m_{\pi^\pm} =$

139.57 MeV/c^2). The pion peak is in fact a mixture of pions and muons as the decay of the former preserves momentum. Only the events corresponding to the middle peak are selected for this analysis as different particle types would lead to different energy deposition pattern.

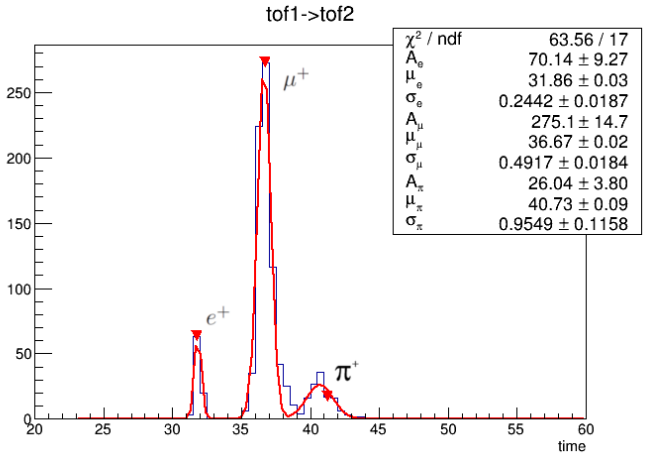

Figure 9.2: Time of flight between TOF1 and TOF2 in nanoseconds. The leftmost peak, the fastest, corresponds to particles that travel very close to the speed of light (e^+, e^-), while the two others are the muon and pion peaks.

Furthermore, only the primary particle tracks are used. The decay products of the muons (e^+, e^-) have different energy and have a much broader angular distribution as they can cover the entire sphere of solid angles. This would result in a lot of planes regularly being hit in way more than 2 bars.

Finally, a minimum of 10 hits is requested for the track to be included. The trigger used in MICE is based on a single hit in TOF1, which doesn't always give a full length track in the EMR. This cut rejects any noise or other events that could possibly have fallen between the cracks.

9.4 Processing

First of all, the raw data samples are reconstructed, i.e. the primary tracks are separated from the noise by time association and the secondary tracks are isolated in an array for further processing.

A distribution of the amount of hits recorded is stored in a histogram for each plane. Moreover, each time a plane is missed by a track, i.e no signal is produced in one plane even though it is on the path of a particle, its plane ID is recorded

The two settings with energies inferior to the threshold for muons to go through the whole detector have been combined into one to increase the level of statistics. It is very rare as we will soon unravel to have a plane missed and that is why, to improve the accuracy of the efficiency measurement, it is critical to have a lot of events. The same thing has been done with the two above threshold. The amount of times each plane was hit after combining the samples above threshold neighboured 3000.

9.5 Results

9.5.1 Signal production

In a real situation, we measure a Time over Threshold in the MAPMT and a charge in the SAPMT. The one that we are interested in for this analysis is the MAPMT as it is the device that provides us with bar hits. The SAPMT efficiency wasn't included as the photomultipliers will be replaced by the end of 2014 and an analysis will be performed then.

These quantities depend on a lot of digitization parameters that determine the ToT and charge measured as a function of the energy initially deposited. To estimate the probability that a given energy deposition will actually be recorded, we use the Monte Carlo sample described above. It provides us with the exact energy deposition for each bar, value that we than digitize according to the following process:

1. Convert energy into number of scintillating photons n_{sph}: 2000 ph/MeV;
2. Sample n_{sph} with a Poisson distribution;
3. Convert n_{sph} into number of trapped photons n_{tph}: $E_T = 2\%$;
4. Sample n_{tph} with a Poisson distribution;
5. Reduce n_{tph} according to the length of Wavelength Shifting Fibres (WLSf) and Clear Fibres (CLf) to get the number of attenuated photons n_{aph}: WLSf -2.0 dB/m, CLf -0.25 dB/m;
6. Apply connector attenuation map: light loss up to 30% in the connector;
7. Sample n_{aph} with a Poisson distribution;
8. Convert n_{aph} to the number of photoelectrons n_{pe}: QE = 20 %;
9. Sample n_{pe} with a Poisson distribution;
10. Correct n_{pe} for cathode non-uniformity: up to 40%;
11. Convert n_{pe} to the number of ADC counts n_{ADC}: 8 ADC counts/n_{pe};
12. Simulate electronics response, Gaussian smearing: $\sigma = 10$ ADC counts;
13. Convert n_{ADC} to ToT: $n_{ADC} = a + b \times \log(ToT/c + d)$;
14. Convert Geant4 time to ADC counts Δt: 2.5 ns/ADC count;
15. Sample Δt with Gaussian distribution: $\sigma = 2$ ADC counts.

If the energy initially deposited in the detector is not high enough, the light yielded and transferred could be too dim to extract a photoelectron from the MAPMT cathode. In that case, no hit would be recorded by the DAQ system.

For each bar in the EMR, we record the energy deposited and the digitized ToT signal. If the latter is zero, even though the former was non-zero, the energy deposited is lost. In fig. 9.3 is plotted the probability that a signal is recorded a function of the energy initially deposited in a given bar. We clearly see that above 1 MeV, approximatively no signal is lost.

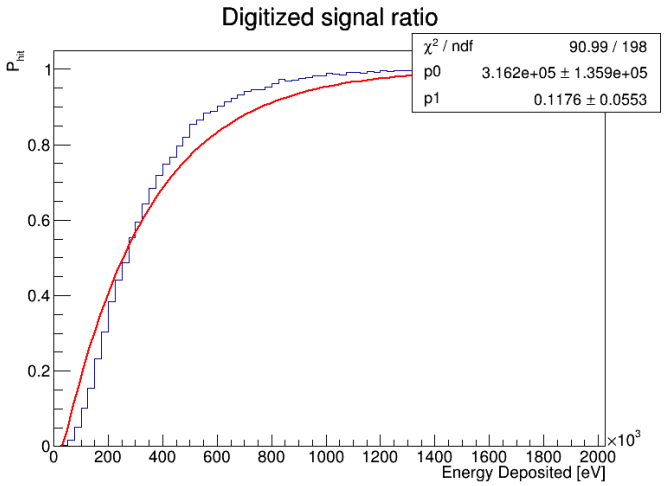

Figure 9.3: Probability that a hit will create a signal after DAQ as function of the energy deposited in the scintillating bar.

In the EMR, due to the triangular shape of the scintillating bars, we can say that a particle always goes through at least two of them in each plane. In the case of beam data where the trajectories are generally perpendicular to the planes, we can go further and say that they hit exactly two bars. In an optimal situation, the distribution of bars hit per plane should be a single bin corresponding to two bars. Nevertheless, several phenomenons can come in the way of that type of distribution. As demonstrated by fig. 9.3, not every hit produces a signal recorded by the DAQ program. That is, one of the hits can be lost depending on the position of the beam with respect to the bars. The energy deposition as a function of the position of the trajectory with respect to the bar has been computed for MIPs using a Geant4 simulation in a previous analysis [65] and is depicted in fig. 9.4.

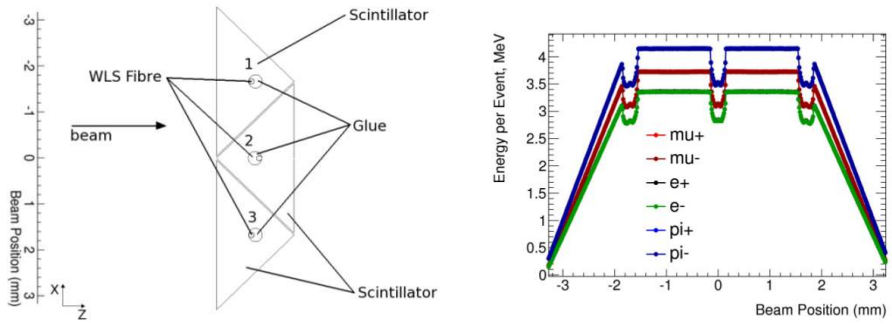

Figure 9.4: EMR simulation of the correlation between position and energy deposition, here represented for 3 adjacent bars [65].

If we combine these results with the probability of producing a hit as a function of the energy, we yield the probability of producing a hit as a function

of the position. What is really interesting is to evaluate the probability of having two bars hit as a function of the position of the beam with respect to two given bars. To achieve this goal, we fit the digitized signal ratio with a probability of the form

$$f_{hit}(E) = 1 - \exp(-E/p_0 + p_1)\,, \tag{9.1}$$

where p_0 and p_1 are the fitting parameters. The base of the triangular section of a bar measures 33 mm which means that the energy deposition will increase linearly from 0 to 16.5 mm away from the edge of the bar. Using Monte Carlo simulation, we can simplify the situation by neglecting the presence of a hole and estimate that $E = p_2 \times x$ with $p_2 \simeq 4.2/16.5 \simeq 0.25$ MeV/mm. If we introduce that definition in the previous one, we get

$$f_{hit}(x) = 1 - \exp(-p_2 \times x/p_0 + p_1)\,, \tag{9.2}$$

which is the probability of having a hit in one bar as a function of the distance from the edge of it. To yield the probability of having two bars hit, the function in eq. 9.2 is combined with its symmetrical equivalent (maximal at 0, minimal at 16.5 mm), i.e.

$$f_{2hits}(x) = (1 - \exp(-p_2 \times x/p_0 + p_1))(1 - \exp(p_2 \times (x - 16.5)/p_0 + p_1)). \tag{9.3}$$

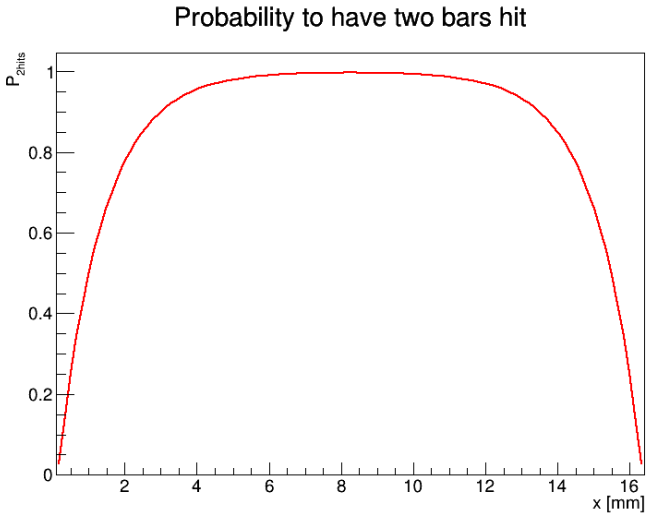

Figure 9.5: Probability to have two hits in one plane

This probability density function is depicted in fig. 9.5. It appears clearly that, when we approach the centre of one of the two bars, the probability of having two hits drops as most of the energy is deposited in one of the two. This pattern is repeated all the way to the edges of the plane where a bar obviously has to be semi-isolated. Nevertheless, the beam is unlikely to go that far and we'll consider for this analysis that it cannot. In light of this, averaging f_{2hits}

over 16.5 mm is equivalent to averaging the probability over the whole plane. The probability of producing two hits in one plane hence reads

$$P_{2hits} = \frac{1}{16.5}\int_0^{16.5} f_{2hits}(x)dx = 84.18\%. \tag{9.4}$$

In fact, we will see in the subsequent parts of the analysis that the low energy events are way less represented than our simulation would suggest. This obviously results in a much higher proportion of single bar hits. Moreover, 3 bars or more hit are theoretically impossible but not with real data. Crosstalk and noisy channels are always around the corner to create a 3rd, 4th, etc. Finally, in our simple estimation, missed planes don't exist. Unfortunately, it would be too good to be true and doesn't account for several irregularity that we can encounter as we will see in the next section.

9.5.2 Global Efficiency

To compute the general efficiency of the detector E_{SA}, only the data samples above threshold should be used. The samples under threshold would provide us with a biased value of the efficiency as the energy deposited is function of the depth. The plane in which the muon stops yields way more light which makes it less likely to not create a signal. Moreover, more energy increases the likelihood of crosstalk as demonstrated in section 7. When a muon goes through the whole detector, the energy deposited in each plane is more or less constant. In addition, all the planes are included and not only the first 60%.

The distribution of the amount of bars hit per plane is given in terms of fraction of the sample R in fig. 9.6 for the samples beneath and beyond threshold. We can clearly see that, when the muon stops in the detector, more planes record high numbers of bars hit and the probability of missing a plane decreases.

As long as at least one hit is recorded in each plane on the path of the particle, it is good enough to have a pair of coordinates per module. Therefore, the efficiency of the detector boils down to

$$\boxed{E_{SA} = 1 - R_0 = 99.57 \pm 0.02\,\%} \tag{9.5}$$

We can yield additional information on the detector by observing the distribution of bars hit for the two types of settings. It appears clearly that, at lower beam momentum, as the muons deposit more energy and stop in the detector, the proportion of planes hit twice is 6% higher. Moreover, higher bar counts are much more likely for low momentum muons, not only because they stop in the detector, but also because they produce more crosstalk on their path. The crosstalk probability increases exponentially as a function of the Time over Threshold as we get from fig. 7.13. Finally, the the percentage of missed bars is even lower for the same set of reasons.

The percentage of single bars we measure can be translated in simulation by applying a cut off at 800 keV of energy deposition. Anything below this value is simply not recorded by the DAQ program. Including this postulate in the Monte Carlo digitization, the probability becomes $P_{2hits} \simeq 61.3\%$, which is much closer to the truth, considering that we neglect the presence of higher number of bars hit.

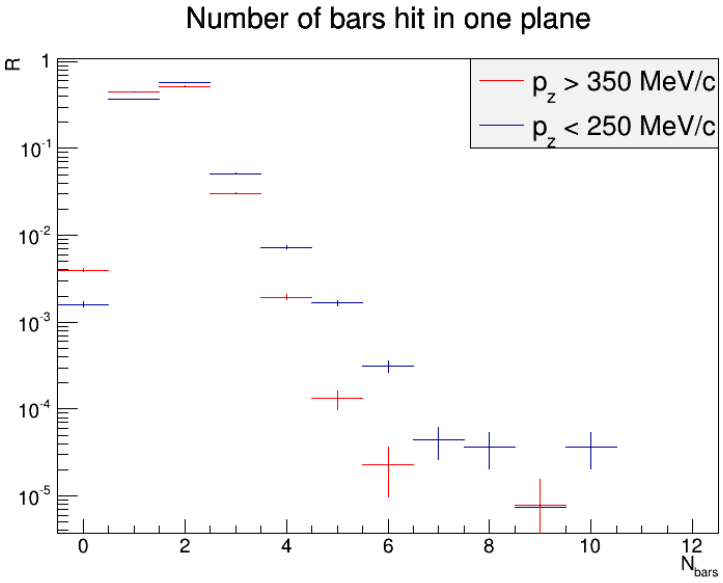

Number of bars	$p_z > 350$ MeV/c	$p_z < 250$ MeV/c
0	0.43 ± 0.02 %	0.16 ± 0.01 %
1	45.25 ± 0.25 %	36.62 ± 0.19 %
2	51.22 ± 0.27 %	57.16 ± 0.26 %
3	2.90 ± 0.05 %	5.13 ± 0.06 %
4	0.18 ± 0.01 %	0.73 ± 0.02 %
5	0.011 ± 0.003 %	0.17 ± 0.01 %
≥ 6	< 0.01 %	< 0.1 %

Figure 9.6: Fraction of the sample that hit a given number of bars per plane

The percentage of planes hit only once is quite high. It won't influence the resolution on the range but will affect the energy reconstruction as some of the energy deposited is purely and simply lost. The percentage of plane missed on the other hand is staggeringly low as we would expect.

9.5.3 Single plane Efficiency

In the current set-up of the EMR, all of the MAPMT are set to the same voltage: 700 V. No high voltage scan has been performed, yet. As the photomultipliers are not all perfectly similar, this could lead to some of them loosing more signals than others or some of them being too sensitive, i.e. recording signals that don't correspond to a particle trail (e.g. crosstalk).

To investigate this phenomenon, the signal acquisition efficiency E_{SA}, alongside the number of bars hit on average in one plane, is a tool of choice. If an MAPMT is set on a voltage too low, the corresponding plane will have a higher percentage of single hit and will miss particles more frequently. If, on the other hand, the voltage is too high, the probability to have more than two hits will rise. In an ideal situation, one would want to maximize the efficiency and keep the amount of planes hit more than twice to a minimum.

To begin with, we take a look the probability of missing a plane R_0 (that

is, $1 - E_{SA}$) as a function of the plane ID (fig. 9.7). We obviously only include the samples with beam moment $p_z > 350$ MeV for the same reasons as exposed the previous sections.

It is apparent that the measured ratio R_0 is very plane dependant as we would expect. Some planes always produce at least a hit on track whereas some of them are lost as frequently as 2.5 % of the time. This indicates that some the MAPMT don't have a perfectly suited voltage supply. The efficiency, however, never falls under 97.5 %, which is fairly satisfactory. Nevertheless, a high voltage scan should be performed by the end of 2014 to optimize the power supply to fit the specifics of each MAPMT.

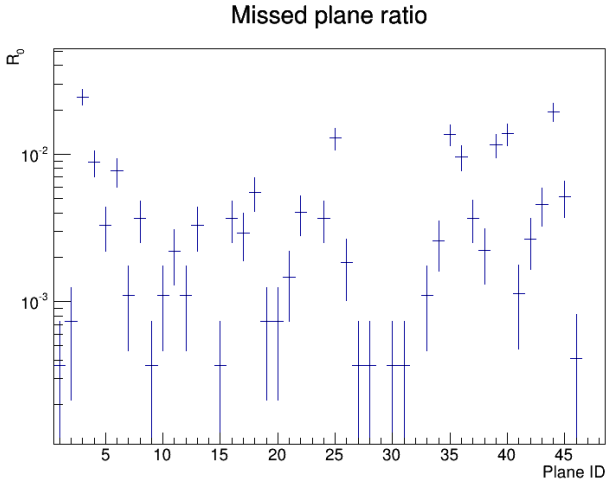

Probability	Number of planes
$R_0 > 1$ %	6
0.1 % $< R_0 <$ 1 %	25
$0 < R_0 <$ 0.1 %	11
$R_0 = 0$	6

Figure 9.7: Probability for a given plane to not produce a signal

9.5.4 Energy dependency

The last important question to answer is how can the energy deposition influence the number of bars hit in one plane. In this section, all the energy settings will be used.

First of all, we observe the behaviour of the different planes when subjected to a high energy beam. In this case, the energy deposition in each plane is relatively similar to the others as we are in the MIP framework for all of them. In fig. 9.8, we see the distribution of bars hit for each plane and the average number of bars hit.

We can see small variations between the different planes which correspond to the relative efficiency of each MAPMT, the voltage chosen, fibre mask misalignment, etc. There is a strong correlation between the planes that have a high number of bars on average ($\overline{N_{bars}} > 1.75$) and the crosstalk level. This is what

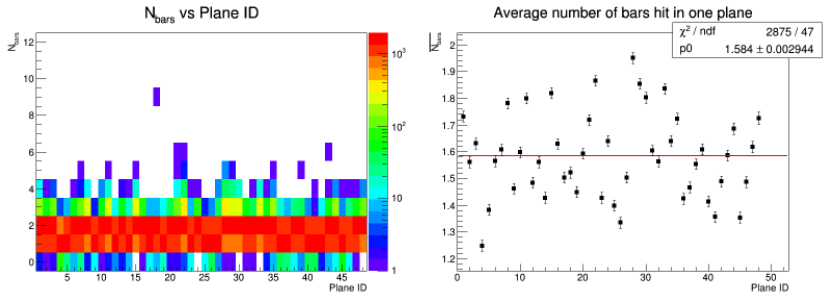

(a) (b)

Figure 9.8: High momentum bar multiplicity: (a) distribution, (b) average.

we would expect as they are both directly proportional to the MAPMT sensitivity and the misalignment. It would be wise to adjust some of the MAPMT voltage to tackle this phenomenon. The positive aspect of these occurrences is that they are less likely to not produce any hit at all.

Finally, we observe how a plane reacts to a very high energy deposition, for instance, a muon stopping in the detector. In fig. 9.9, we see the distribution of bars hit for each plane and the average number of bars hit.

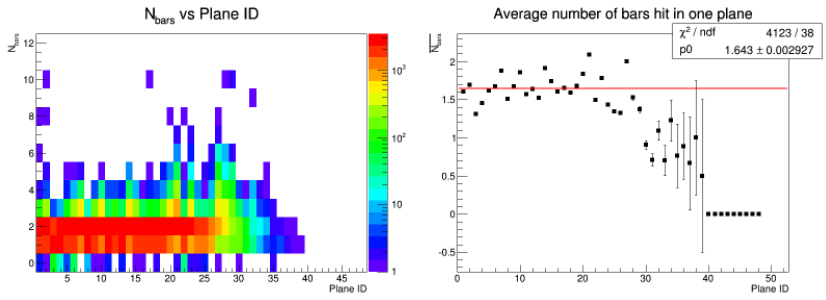

(a) (b)

Figure 9.9: Low momentum bar multiplicity: (a) distribution, (b) average.

The average of all bars is shifted higher as we can tell by the linear fit of the sample, effect of the lower energy beam energy deposition. In addition, when we take a look at the distribution of bars hit for the different planes, we notice a structural modification at the right end of the plot. Where the particle stops, it releases a burst of light that leaks in a lot of channels surrounding the stopping point. As a result, if we take a close look at plane 26 for instance, the probability to have 3 or 4 bars is much higher than to have 1. Moreover, hitting an even bigger amount is no rare phenomenon and we clearly observe a peak in the distribution at the level of this plane and the surrounding ones.

This signal multiplicity pattern is not a surprise. It smears the energy of a single particle in several channels which makes it less straight forward to reconstruct a single point. Nevertheless, the scintillation light in the main channel is always the brightest and we can choose the highest signal as the coordinate of the particle in that plane to keep a good range reconstruction accuracy.

Conclusions

While the analyses performed in the context of this Master Thesis don't guarantee the performance and electron rejection efficiency of the EMR, they nevertheless provide very promising results.

On a purely technical point of view, only 4 of the 2832 channels of the EMR (0.15 %) are not functioning. Moreover, they are on the edge of the fiducial volume and in one the deepest planes, which should not influence the efficiency of the detector on a beam line. The 48 sets of front end electronics integrated in each plane are all functioning as expected and have proved their worth in the context of a proper MICE run session in October 2013. The deviation from the average luminosity that was measured is within range which means that none of the fibres are suspected to be broken and that the connector system implemented to solve the problem works.

When taking a closer look at the machine to unveil any misconceptions, one finds himself surprisingly satisfied with his discoveries as nothing seems to indicate any alarming design flaws. The mismatch channel analysis only revealed two swapped fibres, an outstandingly low number considering that a little under 6000 cables had to be plugged in manually during the assembly of the detector. In addition, the tagging of the two channels in question allows us to easily fix the problem by correcting the DAQ channel map of the EMR.

The investigation of the crosstalk in the MAPMT and their misalignment with respect to the fibre bundle revealed decently low rates of crosstalk while none of the 48 photomultipliers misalignments were within acceptable values. The probability of crosstalk at MIP energy is mostly kept comfortably beneath 0.5 % while the crosstalk signal intensity revolves around 4.5 ± 1.5 %.

The final step that consisted in the evaluation of the signal acquisition efficiency didn't disappoint either, as 99.73 ± 0.02 % of the 130000 planes hit in the analysis produced a recorded signal in the MAPMT. The procedure however revealed a non-negligible asymmetry between the different photomultipliers that will have to be subjected to a high voltage scan in the months to come in order to maximize their efficiency.

The final word about the EMR hardware characterization is that it works beautifully and is on the right path to perform as foreseen in the MICE cooling channel.

On a personal note, this Master Thesis taught me a great deal about the work of a particle physicist: the frustration in the constant technical and programming challenges to overcome, the unquenchable satisfaction of finding what we seek and the everlasting thrilling wonder of what is yet to be discovered. Special thanks to Prof. Alain Blondel for the opportunity of being part of a fantastic international effort to develop the particle physics of tomorrow and to Ruslan Asfandiyarov and Yordan Karadzhov for chaperoning me along in the last year and teaching me how to be a physicist.

References

[1] V. M. Lobashev *et al. Direct Search for the Mass of Neutrino and Anomaly in the Tritium Beta-Spectrum: Status of Troitsk Neutrino Mass Experiment.* Nucl. Instr. and Meth. in Phys. Res. B (Proc. Suppl.) 91:280286. 2001.

[2] R. Davis. *Nobel Lecture: A half-century with solar neutrinos.* Review of Modern Physics 75: 985994. 2003.

[3] R. M. Bionta *et al. Observation of a neutrino burst in coincidence with Supernova 1987A in the Large Magellanic Cloud.* Phys. Rev. Lett. 58: 14941496. 1987.

[4] B. Eberle. *Big Bang Relic Neutrinos and Their Detection.* PhD Thesis, University of Hamburg. 2005.

[5] M. C. Gonzalez-Garcia and Y. Nir. *Neutrino masses and mixing: evidence and implications.* Review of Modern Physics 75: 345402. 2003.

[6] T. Araki *et al. Experimental investigation of geologically produced antineutrinos with KAMLAND.* Nature 436: 499503. 2005.

[7] C. Bemporad *et al. Reactor-based neutrino oscillation experiments.* Review of Modern Physics 74: 297328. 2002.

[8] H. R. Crane. *The Energy and Momentum Relations in the Beta-Decay, and the Search of the Neutrino.* Rev. of Mod. Phys. 20, 1: 278295. 1948.

[9] W. Pauli. *Letter to a physicists gathering at Tubingen, December 4, 1930.* Reprinted in Wolfgang Pauli, Collected Scientific Papers vol. 2, ed. R. Kronig and V. Weisskopf: 1313. 1964.

[10] F. L. Wilson *Fermi's Theory of Beta Decay.* American Journal of Physics, Volume 36, Number 12. 1968.

[11] C. L. Cowan Jr., F. Reines, F. B. Harrison, H. W. Kruse, A. D. McGuire. *Detection of the Free Neutrino: a Confirmation.* Science 124 (3212): 1034. 1956.

[12] M. Goldhaber *et al. Helicity of neutrino.* Phys. Rev. 109: 10151017. 1958.

[13] G. Danby *et al. Observation of high-energy neutrino reactions and the existence of two kinds of neutrinos.* Phys. Rev. Lett. 9: 3644. 1962.

[14] K. Kodama *et al. Observation of tau-neutrino interactions.* Phys. Lett. B 504: 218224. 2001.

[15] B. T. Cleveland *et al. Measurement of the solar electron neutrino flux with the Homestake chlorine detector.* Astrophys. Journal 496: 505526. 1998.

[16] K. Eguchi *et al. First results from KAMLAND: evidence for reactor antineutrino disappearance.* Phys. Rev. Lett. 90, 2: 021802. 2003.

[17] S. Bilenky, B. Pontecorvo. *Lepton mixing and neutrino oscillations* Zh. Eksp. Teor. Fiz., 34, 247. 1957.

[18] Z. Maki *et al. Remarks on the Unified Model of Elementary Particles.* Prog. Theor. Phys. 28: 870880. 1962.

[19] J. N. Bahcall *et al. Present Status of the Theoretical Predictions for the* ^{36}Cl *Solar-Neutrino Experiment.* Phys. Rev. Lett. 20: 12091212. 1968.

[20] SAGE Collaboration. *Measurement of the solar neutrino capture rate with gallium metal.* Phys. Rev. C 60: 055801. 1999.

[21] W. Hampel *et al. GALLEX solar neutrino observations: results for GALLEX IV.* Phys. Lett. B 447: 127133. 1999.

[22] The SNO Collaboration. *Measurements of the rate of* $\nu_e + d \rightarrow p + p + e^-$ *interactions produced by* ^8B *solar neutrinos at the Sudbury Neutrino Observatory.* Phys. Rev. Lett. 87: 071301. 2001.

[23] Y. Fukuda *et al. Evidence for Oscillation of Atmospheric Neutrinos.* Phys. Rev. Lett. 81: 15621567. 1998.

[24] T2K Collaboration. *Measurement of Neutrino Oscillation Parameters from Muon Neutrino Disappearance with an Off-axis Beam.* Phys. Rev. Lett. 111, 211803. 2013.

[25] Y. Abe *et al. Reactor electron antineutrino disappearance in the Double Chooz experiment* Phys. Rev. D 86, 052008. 2012.

[26] D. V. Forero, M. Trtola, J. W. F. Valle *Global status of neutrino oscillation parameters after Neutrino-2012.* Phys. Rev. D 86, 073012. 2012.

[27] J. Beringer *et al.* [Particle Data Group]. *Review of Particle Physics.* Phys. Rev. D 86, 010001. 2012.

[28] V. N. Gribov, B. Pontecorvo. *Neutrino astronomy and lepton charge.* Physics Letters B28: 493. 1969

[29] MICE Collaboration. *An International Muon Ionization Cooling Experiment (MICE).* Proposal to the Rutherford Appleton Laboratory, 2003.

[30] F. J. P. Soler, C. D. Froggatt, F. Muheim. *Neutrinos in Particle Physics, Astrophysics and Cosmology.* CRC Press, Taylor and Francis Group. 2009.

[31] C. Albright *et al. Physics at a Neutrino Factory.* Fermilab-FN-692, arXiv:hep-ex/0008064. 2000.

[32] G.I. Budker, in Proc. of the 7th Int. Conf. on High Energy Accelerators. Yerevan. 1969.

[33] S. Ozaki, R. Palmer, M. Zisman, J. Gallardo. *Feasibility Study-II of a Muon-Based Neutrino Source.* Eds. BNL-52623. 2001.

[34] K. Hanke. *Muon Front-End without Cooling.* NuFact Note 59. 2000.

[35] A. De Rujula, M. B. Gavela, P. Hernandez. *Neutrino oscillation physics with a neutrino factory.* Nucl. Phys. B 547: 21. 1999.

[36] A. Yu. Smirnov. *The MSW effect and Solar Neutrinos.* arXiv:hep-ph/0305106. 2003.

[37] M. Lindner. *The Physics Potential of Future Long Baseline Neutrino Oscillation Experiments.* Springer Tracts Mod. Phys. 190: 209242. 2003.

[38] P. Huber *et al. Synergies between the first-generation JHF-SK and NuMI superbeam experiments.* Nucl. Phys. B 654: 329. 2003

[39] Y. Itow *et al. The JHF-Kamioka neutrino project.* KEK report 2001-4: ICRRreport47720017. 2001.

[40] G. Prior. *Status of the Neutrino Factory accelerator design studies.* J. Phys.: Conf. Ser. 408 012013. 2013.

[41] A. N. Skrinskii and V. V. Parkhomchuk. *Method of cooling beams of charged particles.* Sov. J. Part. Nucl. 12(3): 223247. 1981.

[42] P. Sigmund. *Particle Radiation and Radiation Effects.* Springer Series in Solid State Sciences, 151. Berlin Heidelberg: Springer-Verlag. ISBN 3-540-31713-9. 2006.

[43] R. P. Johnson. *Ionization Cooling and Muon Colliders.* Proceedings of EPAC08, Genova, Italy. 2008.

[44] The $\mu^+\mu^-$ Collaboration. *Muon Muon Collider: a feasibility study.* BNL 52503. 1997.

[45] M. Apollonio *et al. The MICE diffuser system.* Proceedings of EPAC08, Genova, Italy. 2008.

[46] D. Li *et al. A 201-MHz normal conductig RF cavity for the International MICE Experiment.* Proceedings of EPAC08, Genova, Italy. 2008.

[47] M. Bonesini *et al. The design and commissioning of the MICE upstream Time-Of-Flight system.* Nucl. Instr. and Meth. in Phys. Res. A 615: 1426. 2010.

[48] L. Cremaldi *et al. A Cherenkov Radiation Detector with High Density Aerogels.* IEEE Transactions on Nuclear Science 56: 14751478. 2009.

[49] M. Bonesini and M. Rayner. [MICE Collaboration] *The MICE PID Detector System.* MICE Note 304. 2010.

[50] M. Ellis *et al.* [MICE Collaboration] *The design, construction and performance of the MICE scintillating fibre trackers.* MICE-NOTE-DAQ-254. 2010.

[51] J. Lee-Franzini *et al. The KLOE electromagnetic calorimeter.* Nucl. Instr. and Meth. in Phys. Res. A 360: 201205. 1995.

[52] A. R. Sandström. *Background and Instrumentations in MICE.* PhD Thesis, University of Geneva. 2007.

[53] R. Asfandiyarov *et al.* [MICE Collaboration]. *Selecting Philips XP 2972 Photomultiplier Tubes for the Electron Muon Ranger (EMR).* MICE-NOTE-DAQ-383. 2012.

[54] A. Alekou. [MICE Collaboration] *MICE Status.* MICE-NOTE-DAQ-297. 2010.

[55] A. Pla-Dalmau *et al. Low-cost extruded plastic scintillator.* Nucl. Instr. and Meth. in Phys. Res. A 466: 482491. 2001.

[56] Saint-Gobain Crystals. *Scintillating Products: Scintillating Optical Fibres.* Saint-Gobain Ceramics and Plastics, Inc. 2005.

[57] *Kuraray Scintillation Materials.* http://www.hamamatsu.com/resources/pdf/etd/H7546A_H7546B_TPMH1240E12.pdf. 2007.

[58] R. Asfandiyarov *et al.* [MICE Collaboration]. *Modifications to EMR Design.* MICE-NOTE-DAQ-357. 2011.

[59] R. Asfandiyarov *et al.* [MICE Collaboration]. *Electron-Muon Ranger (EMR) Construction and Tests.* MICE Collaboration Meeting 29. 2011.

[60] *Multianode Photomultiplier Tube Assembly H7546A, H7546B.* http://www.phenix.bnl.gov/WWW/publish/donlynch/RXNP/Safety%20Review%206_22_06/Kuraray-PSF-Y11.pdf. 2008.

[61] R. Asfandiyarov *et al.* [MICE Collaboration]. *Features of CAEN V1731 Flash ADC Waveform Digitizer.* MICE-NOTE-DAQ-358. 2011.

[62] F. Drielsma *et al.* [MICE Collaboration] *Electron Muon Ranger (EMR) Electronics Quality Tests.* MICE-NOTE-DAQ-441. 2013.

[63] *Hamamatsu Handbook, Chapter 9 : Position Sensitive Photomultiplier Tubes.* http://www.hamamatsu.com/resources/pdf/etd/PMT_handbook_v3aE-Chapter9.pdf. 2006.

[64] F. Drielsma *et al.* [MICE Collaboration] *Crosstalk and Misalignment in the Electron Muon Ranger (EMR)* MICE-NOTE-DAQ-440. 2013.

[65] R. Asfandiyarov *et al.* [MICE Collaboration] *Geant4 Simulation of the EMR Detector Response Study.* 2012.

[66] *The MICE Experiment: Momentum Measurements Using the Time of Flight Counters.* http://www2.warwick.ac.uk/fac/sci/physics/research/epp/meetings/uknf08/programme/mice/UKNFMICE_Rayner.pdf. 2008.